Università di Pisa

Facoltà di Scienze Matematiche Fisiche e Naturali

Corso di Laurea Specialistica in Scienze Fisiche

Anno Accademico 2005/2006

Tesi di Laurea Specialistica

LATTICE DESIGN FOR ILC COMPTON RING

Candidato
Erminia Bressi

Relatore
Chiar.mo Prof. Franco Cervelli

Co relatore
Chiar.ma Prof.ssa Susanna Guiducci

Contents

Introduction

In the last twenty years the construction of dedicated particle accelerators has given an important contribution to the particle physics development.

At present, the scientific community is going to prepare itself for a new challenge: the International Linear Accelerator (ILC), that will engage Asia, Europe and USA. While LHC will explorate the TeV energy scale through pp interactions, ILC will continue the researches through the elementary e^+e^- interaction. The peculiarity of this new linear accelerator will be the very high luminosity at the interaction point ($\sim 2 \times 10^{34}$ cm^{-2}s^{-1}). The clean signatures and the precise measurements are made possible by a high-luminosity linear collider at a known and tunable beam energy, so bringing revolutionary new insights into the fundamental interaction physics. ILC is expected to solve Standard Model 'open questions', and to investigate new theories like Supersymmetry.

Recent studies [1] [2] have shown that the full potential of ILC can be exploited only using polarized beams.

In the first chapter of this thesis the physical importance of beams polarized at ILC is overviewed.

In the ILC design an important problem is the choice of the best polarized positron source. In Chapter 2, two schemes are presented to obtain polarized positrons: a) undulator-based positron source and b) Compton source. In both schemes circularly polarized photons are produced and then are converted into polarized positrons in a relatively thin target. The choice between these two solutions is still under discussion and many simulations are going on in order to get a decision.

In this thesis the 'Compton' proposal is considered in detail. The main element of this scheme is the so called Compton ring, i.e. an electron storage ring, where the Compton interaction between the electron beam and a laser produces circularly polarized photons. Chapter 3 and 4 deal with a proposal for a Compton Ring lattice, that has been designed using a specialized CAD program (MAD).

Chapter 5 presents the study of the longitudinal beam dynamics due to the laser interaction with the beam in the Compton ring. The beam stability is analized for the lattice models discussed in Chapter 4.

The Compton Ring idea has been also proposed for the CLIC (Compact LInear Collider) polarized positron source [3]. CLIC differs from ILC in several beam parameters (damping ring, bunch spacing, repetition rate); as a consequence several aspects of the positron source at CLIC are easier than at ILC. The studies presented in this thesis could be particularly useful not only for ILC but also for CLIC layout.

The results presented in this thesis are encouraging. Anyway many improvements are still necessary in order to optimize the 'Compton scheme'.

Chapter 1

ILC motivations

The first exploration of the TeV energy scale will be made with the proton-proton Large Hadron Collider (LHC), which is scheduled to start operation on next year (2007). It will deliver luminosity to four experiments (ATLAS, CMS, LHC-b, ALICE), that will investigate important open questions about particle physics.

Its discovery potential is expected to be complemented by the electron-positron International Linear Collider (ILC), the new project of the scientific community. The clean signatures and the precise measurements are made possible by a high-luminosity linear collider at a known and tunable beam energy and could bring revolutionary new insights into our understanding of the structure of matter, space and time. In fact, in addition to detailed studies of directly accessible new particles, it would also make possible indirect searches for new physics with high sensitivity in a largely model-independent approach [5]. In the hunt for physics beyond the Standard Model, only small signals may be visible, and a linear collider provides optimal conditions for searching for the unexpected.

In a linear collider polarized beams give the possibility to maximize the physics return: this is true even more, considering that a high degree of polarization can be realized without a significant loss in luminosity. In the recent past the availability of a polarized beam at the SLC (SLAC Linear Collider) compensated, in some respects, for the fact that it had a lower

luminosity than LEP (Large Electron Positron collider). In the same period of HERA (Hadron-Elektron-Ring-Anlage), polarized lepton scattering has provided surprising revelations in hadronic structure. Polarized beams play also a crucial role in the experimental programmes of RHIC (Relativistic Heavy Ion Collider).

At ILC, a polarized electron beam would already provide a valuable tool for accurate tests of the Standard Model and for diagnosing new physics. This explains why polarization of the electron beam is already foreseen for the baseline design [4]. A high degree of polarization (at least 80%) is already envisaged, and new results indicate that a 90% polarization should be achievable.

However, as it will be explained later, it will be possible to exploit the full potential of the linear collider only if the positron beam is also polarized.

The dominant processes in e^+e^- experiments are annihilation (s-channel) and scattering (t- and u-channel) processes. In annihilation processes (see Fig. 1.1), the helicities of the electron and positron are coupled to each other by the spin of the particle(s) exchanged in the direct channel. On the contrary, in the scattering diagrams (see Fig. 1.2), the helicities of the incoming beams are directly coupled to the helicities of the final particles.

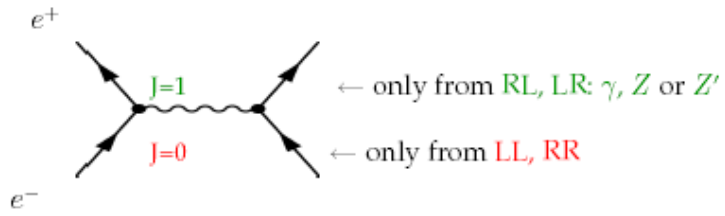

Figure 1.1: Configurations in $s-$channel diagrams. The recombination into a vector particle (J=1) is given by the LR and RL configurations, while the recombination into a scalar particle (J=0) is due to LL or RR configurations.

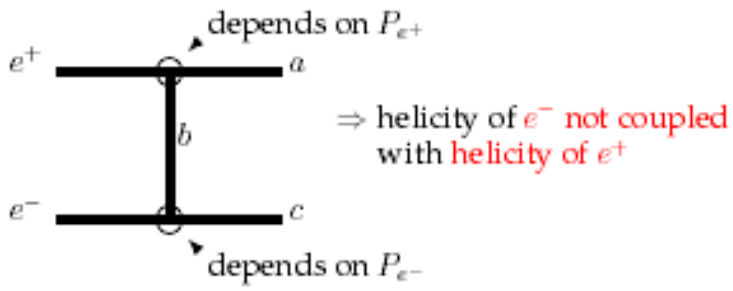

Figure 1.2: Configurations in $t-$ and $u-$channel diagrams. The helicity of the incoming beam is directly coupled to the helicity of the final particle and is completely independent of the helicity of the second incoming particle.

Suitable combinations of the electron and positron beam polarizations may therefore be used to enhance considerably signal rates and also to efficiently suppress unwanted background processes. These aspects are particularly important when searching for new physics, expected to show up with very small rates. Therefore, an increased signal/background ratio, combined with large luminosity, gives additional opportunities for possible discoveries. The signal/background ratio can be parametrized [5] by a scaling factor comparing the cross sections with two different polarization configurations a and b:

$$\text{scaling factor} = \sigma_b/\sigma_a \ , \tag{1.1}$$

where a refers to the annihilation process, and b refers to the scattering processes. When the background process depends on beam polarization in a way different from the expected signal process, one can suppress the background and enhance the signal simultaneously with the suitable polarization configuration of both beams.

On the contrary, in cases where both processes, background and expected signal, show a similar dependence on beam polarization, one has no advantages in the ratio 'signal over background'. However, also in these cases, beams polarization is advantageous because of the immediate gain in sta-

tistical significance. In fact, in order to get a significance of N_σ standard deviations for the new signal (S), it is required that:

$$S > N_\sigma \times \sqrt{B} \ , \tag{1.2}$$

where $\sqrt{B}$ is the statistical variation of the background (B) process (Gaussian distribution assumed, which is suitable thanks to the high statistics at the ILC). As a single example to show the statistical gain, Table 1.1 reports S/B and $S/\sqrt{B}$, for the two cases where the background and signal processes have the same or an inverse scaling factor.

	S	B	S/B	$S/\sqrt{B}$
Example 1	$\times 2$	$\times 0.5$	$\times 4$	$2\sqrt{2}$
Example 2	$\times 2$	$\times 2$	*unchanged*	$\sqrt{2}$

Table 1.1: Examples of the gain in S/B and in $S/\sqrt{B}$

Furthermore, in scattering processes, the helicities of the electron and positron can be related directly to the properties of any produced (new) particles. The ability to adjust independently the polarizations of both beams simultaneously will provide unique possibilities for directly probing the properties of the new particles. In particular, it becomes possible to gain direct access to their quantum numbers and chiral couplings with a minimal number of assumptions. Many models of physics beyond the Standard Model have a large number of free parameters. For example, the Minimal Supersymmetric extension of the Standard Model (MSSM) contains more than one hundred new physical parameters, whose complete determination would require many independent experimental observables. Having both beams polarized would increase significantly the number of measurable observables, providing more powerful diagnostic tools, which could be crucial for determining or constraining many free parameters. The combination of two polarized beams

may not only be important for the discovery of new particles, but may also be indispensable for revealing the structure of the underlying new physics.

1.1 Open questions of the SM

1.1.1 Top physics

The top quark is by far the heaviest fermion observed. All the present experimental results indicate that it behaves as would be expected for a sequential third generation quark. Its large mass, which is close to the scale of electroweak symmetry breaking, makes the top quark a unique object in pinning down the origin of electroweak symmetry breaking [6]. High precision measurements of the top quark properties will be an essential part of the ILC research program. Availability of both beams polarized allows for a substantial improvement in the measurement of the known properties, the couplings determination and limits for non-standard top physics.

The top neutral electroweak couplings are accessible only at lepton colliders, because top quarks at hadron colliders are pair-produced via gluon exchange. Therefore, a linear collider provides an ideal tool to probe the couplings of the top quark to the electroweak gauge bosons.

In particular, detection of the $(\gamma, Z)t\bar{t}$ couplings [2], that are equal to zero in the Standard Model, would be a clear manifestation of new physics.

Different studies [7] have shown that beam polarization effects represent a useful tool in this search. To determine the SM top vector coupling (v_t), one has to measure with high accuracy the $left - right$ asymmetry A_{LR}

$$A_{LR} = \frac{\sigma_{LR} - \sigma_{RL}}{\sigma_{LR} + \sigma_{RL}} \ , \tag{1.3}$$

where σ_{ij} ($i = L, R$ and $j = L, R$) are the cross sections for the different polarization configurations.

With an integrated luminosity of $L_{int} = 300 fb^{-1}$, precisions in A_{LR} and v_t of about 0.4% and 1% respectively, can be achieved at the ILC. Using simultaneously polarized e^- and e^+ beams with $(P_{e^-}, P_{e^+}) = (\mp 80\%, \pm 60\%)$

is more advantageous compared to the case of only polarized electrons with $|P_{e^-}| = 80\%$. In fact ,this leads to a reduction of the relative uncertainty $\Delta A_{LR}/A_{LR}$ by about a factor of 3 [2].

Another interesting example is the Flavour-Changing Neutral (FCN) couplings of the top quark. In fact FCN couplings are relevant to numerous extensions of the SM, and can represent an interesting field for new-physics searches. Limits on top FCN decay branching ratios can be obtained from top-pair production with subsequent $\bar{t}$ decay into γ, Z plus light quark governed by the FCN anomalous tVq couplings

$$e^+e^- \longrightarrow t\bar{t} \longrightarrow W^+bV\bar{q} \ ,$$

where $V = \gamma, Z$ and $q = u, c$, or from single top production

$$e^+e^- \longrightarrow t\bar{q} \longrightarrow W^+b\bar{q} \ ,$$

mediated by the anomalous couplings at the production vertex. Fig. (1.3) shows the Feynmann diagrams for the FCN couplings processes.

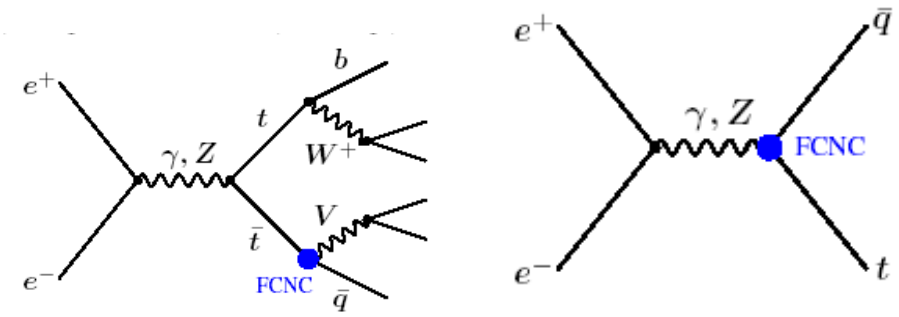

Figure 1.3: Left: Flavour changing neutral coupling in $t\bar{t}$ production. Right: Single top production via Ztq or γtq FCN coupling.

Beam polarization is very efficient in significantly reducing the background and is therefore particulary important in limits obtained from single

top production. With respect to unpolarized beams, having polarization $(80\%, 0)$, decreases the background by a factor of ~ 5 while keeping 90% of the signal [9]. With $(80\%, -45\%)$ the background is reduced by a factor of $1/(1 - P_{e^-})(1 + P_{e^+}) \sim 9$ and the signal is increased by 20% compared to the case of no polarization [9]. In conclusion, S/B and $S/\sqrt{B}$ are improved by factors of 2.1 and 1.7, respectively. Already, as one can see in Table 1.2, with e^- and e^+ polarization $(80\%, 45\%)$, as an example, one improves the $3-\sigma$ discovery limits on the vector (γ^μ) coupling [9] at $\sqrt{s} = 500$ GeV by a factor of 3 (a factor of 1.7 compared to only electron polarization) and the limits on the tensor $(\sigma^{\mu\nu})$ coupling [9] at $\sqrt{s} = 800$ GeV by about a factor 2.6 (a factor 1.8 compared to electron polarization only).

	unpolarized beams	$\lvert P_{e^-}\rvert = 80\%$	$(\lvert P_{e^-}\rvert, \lvert P_{e^+}\rvert) = (80\%, 45\%)$
$\sqrt{s} = 500$GeV			
$BR(t \to Zq)(\gamma_\mu)$	6.1×10^{-4}	3.9×10^{-4}	2.2×10^{-4}
$BR(t \to Zc)(\sigma_{\mu\nu})$	4.8×10^{-5}	3.1×10^{-5}	1.7×10^{-5}
$BR(t \to \gamma q)$	3.0×10^{-5}	1.7×10^{-5}	9.3×10^{-6}
$\sqrt{s} = 800$GeV			
$BR(t \to Zq)(\gamma_\mu)$	5.9×10^{-4}	4.3×10^{-4}	2.3×10^{-4}
$BR(t \to Zc)(\sigma_{\mu\nu})$	1.7×10^{-5}	1.3×10^{-5}	7.0×10^{-6}
$BR(t \to \gamma q)$	1.0×10^{-5}	6.7×10^{-6}	3.6×10^{-6}

Table 1.2: $3-\sigma$ discovery limit on top FCN couplings from top branching fractions at $\sqrt{s} = 500$ GeV with $L_{int} = 300$ fb^{-1} and at $\sqrt{s} = 800$ GeV with $L_{int} = 500$ fb^{-1}.

A more recent study was made for $(|P_{e^-}|, |P_{e^+}|) = (80\%, 60\%)$ at $\sqrt{s} = 500$ GeV with $L_{int} = 345$ fb^{-1} and at $\sqrt{s} = 800$ GeV with $L_{int} = 534$ fb^{-1} [10]. Comparison with the limits for FNC couplings expected at the LHC shows that the ILC measurements are complementary in searches for FCN

couplings. Whereas the LHC can be superior in the discovery potential for γ^μ couplings, the ILC at $\sqrt{s} = 800$ GeV with $(80\%, 60\%)$ may gain an order of magnitude for the discovery of $\sigma^{\mu\nu}$ couplings to the Z and the photon. This is shown in Table 1.3, that reports the $3-\sigma$ discovery limit on top FCN vector (γ_μ) and tensor $(\sigma_{\mu\nu})$ couplings from top decay processes at the LHC and in single top production at the ILC, $\sqrt{s} = 500$ GeV and 800 GeV, for one year of operation.

	LHC	$ILC, \sqrt{s} = 500GeV$	$ILC, \sqrt{s} = 800GeV$
$BR(t \to Zc)(\gamma_\mu)$	3.6×10^{-5}	1.9×10^{-4}	1.9×10^{-4}
$BR(t \to Zc)(\sigma_{\mu\nu})$	3.6×10^{-5}	1.8×10^{-5}	7.2×10^{-6}
$BR(t \to \gamma c)$	1.2×10^{-5}	1×10^{-5}	3.8×10^{-6}

Table 1.3: $3-\sigma$ discovery limit on top FCN couplings that can be obtained from top decay processes at the LHC and in single top production at the ILC, with $(P_{e^-}, P_{e^+}) = (80\%, 60\%)$ for one year of operation.

1.1.2 Higgs physics

One of the major physics goals at the ILC is the precise analysis of all the properties of the Higgs particle. For a light Higgs the two major production processes, Higgs-strahlung ($e^+e^- \longrightarrow HZ$) and WW fusion ($e^+e^- \longrightarrow H\nu\bar{\nu}$) will have similar rates at $\sqrt{s} = 500$ GeV (see Fig. (1.4)).

Beam polarization does not play a key role in determining the Higgs properties; however, it is very helpful for separating the production processes, suppressing the dominant background processes, and improving the accuracy in determining the general couplings.

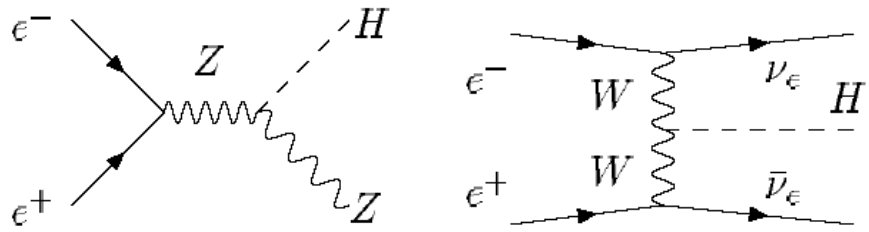

Figure 1.4: Main production mechanism of the SM Higgs boson at the ILC

Configuration (P_{e^-}, P_{e^+})	Scaling factors $e^+e^- \longrightarrow H\nu\bar{\nu}$	Scaling factors $e^+e^- \longrightarrow HZ$
$(+80\%, 0)$	0.20	0.87
$(-80\%, 0)$	1.80	1.13
$(+80\%, -60\%)$	0.08	1.26
$(-80\%, +60\%)$	2.88	1.70

Table 1.4: Higgs production scaling factors (Eq. (1.1)) in the Standard Model at $\sqrt{s} = 500$ GeV for different polarization configurations with regard to the unpolarized case.

Beam polarization can be used to enhance the HZ contribution with respect to the WW fusion signal and vice versa. Table 1.4 shows that there is a gain of a factor $(1.26/0.08)/(0.87/0.20) \sim 4$ in the ratio $\sigma(HZ)/\sigma(H\nu\bar{\nu})$ when left-handed polarized positrons are used in addition to right-handed polarized electrons.

The dominant background processes are:

$$e^+e^- \longrightarrow We\nu_e \ , \qquad e^+e^- \longrightarrow W^+W^-$$

$$e^+e^- \longrightarrow Z\nu_e\bar{\nu}_e \ , \qquad e^+e^- \longrightarrow ZZ$$

that can be suppressed using both polarized beams (see Table 1.5). For example, a factor of 2 can be gained for the WW background suppression.

Configuration (P_{e^-}, P_{e^+})	Scaling factors $e^+e^- \longrightarrow W^+W^-$	Scaling factors $e^+e^- \longrightarrow ZZ$
$(+80\%, 0)$	0.20	0.76
$(-80\%, 0)$	1.80	1.25
$(+80\%, -60\%)$	0.10	1.05
$(-80\%, +60\%)$	2.85	1.91

Table 1.5: Scaling factors of WW and ZZ production at $\sqrt{s} = 500$ GeV for different polarization configurations with regard to the unpolarized case.

1.2 Polarized beams for Supersimmetry studies

1.2.1 Minimal SUSY Model (MSSM)

The polarization of both beams at ILC is relevant for supersymmetry, which is one of the best motivated possibilities for new physics research. If nature is supersymmetric at the electroweak scale, there is a priori a large number of parameters specifying different scenarios. With specific model assumptions about the SUSY breaking mechanism and mass unifications, the number of free parameters is strongly reduced. However, one should keep in mind, that at future experiments at the LHC and the ILC, one has, after detecting signals expected by SUSY, to determine the parameters as model-independently as possible and to confirm the underlying assumptions. This model-indipendent search is well suitable by e^+ and e^- polarized beams.

Supersymmetry associates scalars to chiral (anti)fermions:

$$e^-_{L,R} \longleftrightarrow \tilde{e}^-_{L,R} \quad and \quad e^+_{L,R} \longleftrightarrow \tilde{e}^+_{R,L} \; . \tag{1.4}$$

Therefore an important problem in SUSY searches is to test whether the supersymmetric partners of the electrons/positrons carry the same chiral quantum numbers as their SM partners.

The *selectron* production:

$$e^+e^- \longrightarrow \tilde{e}^+_{L,R}\tilde{e}^-_{L,R} \ . \tag{1.5}$$

can occur in $s-$ and $t-$channel, as Fig. 1.5 shows.

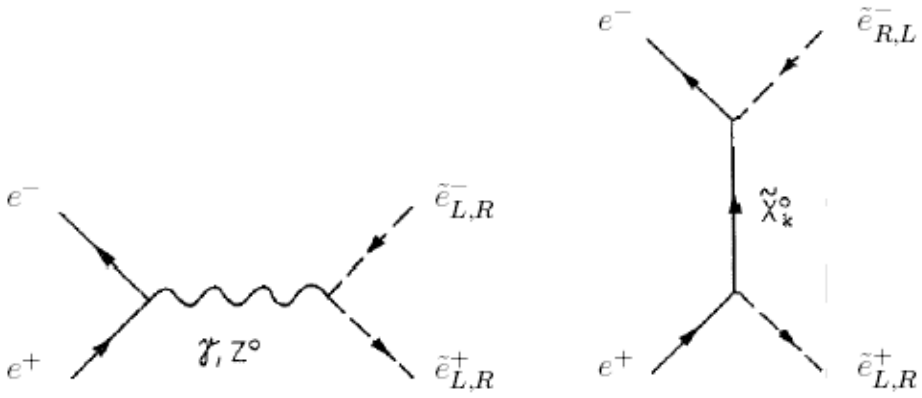

Figure 1.5: Selectron production: $\gamma, Z-$exchange in the s-channel and $\tilde{\chi}^0_1 \ldots \tilde{\chi}^0_4$ -exchange in the t-channel.

In the s-channel the process occurs via γ, Z exchange and only pairs $\tilde{e}^+_L\tilde{e}^-_L, \tilde{e}^+_R\tilde{e}^-_R$ can be produced. On the contrary, in the t-channel the pair productions, $\tilde{e}^+_L\tilde{e}^-_L, \tilde{e}^+_R\tilde{e}^-_R$ and $\tilde{e}^+_L\tilde{e}^-_R, \tilde{e}^+_R\tilde{e}^-_L$, are possible.

Hence, the association between scalars and chiral fermions, can be directly tested only in the t-channel. Polarized beams serve to separate this channel from the s-channel and to enhance the cross section of just those SUSY partners of the initial chiral $e^-_{L,R}$ and $e^+_{L,R}$ given by the beam polarization (see Eq. (1.4)).

The importance of having both beams polarized is demonstrated in Fig. (1.6), which exhibits the isolation of the $\tilde{e}_L^+\tilde{e}_R^-$ pair. It is clear in the figure that an high electron polarization ($P_{e^-} \geq +90\%$) is not enough by itself to disentangle the pairs $\tilde{e}_L^+\tilde{e}_R^-$ and $\tilde{e}_R^+\tilde{e}_R^-$ and to test their association to the chiral quantum numbers. In fact, as one can see in the left panel, their cross sections are numerically very close. Using a polarized positron beam, the pair $\tilde{e}_L^+\tilde{e}_R^-$ can be separated (see the right panel of the same figure).

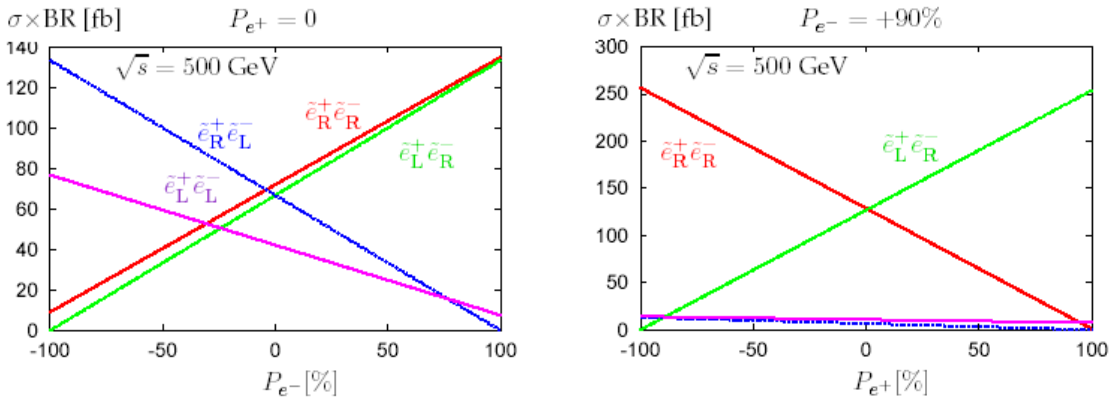

Figure 1.6: Separation of the selectron pair $\tilde{e}_L^+\tilde{e}_R^-$ is not possible with electron polarization only (left panel). If, however, both beams are polarized, the cross sections (right panel) differ and the RR configuration separates the pair $\tilde{e}_L^+\tilde{e}_R^-$

An extesive review of the Physics potential of ILC when using e^+ and e^- polarized beams may be found in [5].

Chapter 2

Polarized positron sources

Two ideas have been studied in detail to obtain polarized positrons: undulator-based positron source and Compton source. In both schemes circularly polarized photons are produced and then converted into polarized positrons in a relatively thin target (~ 0.5 radiation length). These photon-based sources are very different from a 'conventional' positron source (also under consideration for the ILC). The conventional source uses a multi-GeV electron drive beam in conjunction with thick, high$-Z$ targets to produce positrons from the resultant electromagnetic cascade in the target. However, in this case, the produced positrons cannot be polarized.

The photon-based and the conventional schemes present very similar engineering challenges while at the same time having distinct attributes and drawbacks. The big advantage of the conventional source is that it is completely decoupled from the rest of the ILC [5]. The conventional scheme leads to some advantages in commissioning and uptime. However, with careful design photon based of the source, these advantages can result not so relevant.

The photon-based positron source has three advantages over the conventional source:

- in a photon-based source the target can be thinner and therefore it is possible to use lower-Z materials such as Ti-alloys, that are stronger than the W-Re alloys used in the conventional sources;

- the photon energy can be chosen to be lower than the neutron photoproduction cross section and the activation of the target material may be much reduced;

- the emittance of the produced positrons is smaller because the target is thin. This leads to advantages for the positron damping ring design, reducing the cost advantages of the conventional source;

- it is easier to achieve a very large amount of positrons. This is particularly important because the positron charge needed for ILC is a factor 10^3 larger than the one achievable with the conventional positron source of the SLC [23] (that is viewed as the ILC prototype).

2.1 Positron production in the target

When polarized photons interact with the target, they cause a shower developing as a result of a pair creation. For the photon energy range of our interest the Compton and photoelectric effects do not give significant input in the interaction process.

The mostly interesting property of the interaction between the photon and the media is a correlation between the initial photon polarization and the final spins of the produced electron-positron pairs [24]. The spin of the produced particles is related to their energy. So one needs to arrange the energy selection of the produced particles for the arrangement of helicity transferring.

When the positron is created with the maximum energy (i.e. the initial photon energy minus an electron rest mass), the photon polarization transferes completely to the produced positron. However, the positron differential cross section over energy [27] shows that the number of the particles around the maximum energy is small. Hence, the energy acceptance for the collected particles, is the result of a compromise between the required polarization value and the amount of the collected particles.

For example Fig. 2.1 shows the average value of polarization as a function of the ratio between the positron energy and its maximum energy.

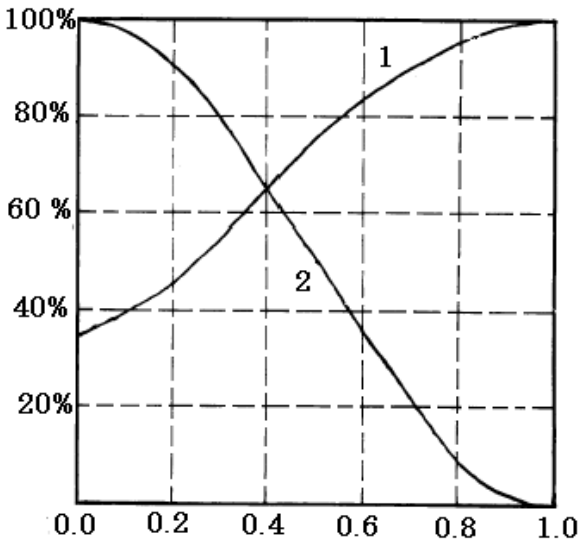

Figure 2.1: Average polarization (curve 1) and the share of positrons (curve 2) as functions of the positron energy over its maximum energy

In this figure, choising the polarization level on curve 1, curve 2 provides the particle yield for a given energy interval. For example, the polarized positrons with ∼80% polarization level (curve 1) are ∼ 40% of all the produced positrons (curve 2); the x axis shows that, to collect these positrons it is necessary to select the positrons with an energy (normalized at the positron maximum energy) equal to 0.6.

Fig. 2.1 is obtained under condition that the initial photon beam has 100% polarization and zero spread over frequencies and in the hypothesis of 10 MeV photons. For a higher photon energy, at a given energy interval of the collected positrons, the polarization degree is higher than the one shown in Fig. 2.1.

As a conclusion the target conversion system can be efficiently working when taking into account the following considerations:

- the circular polarization degree of the primary photon beam is a limiting number for the polarization of the created electrons and positrons, so it is desiderable to have it as high as possible;
- in the photon beam the highest radiation density is required for the purposes of particle selection with the necessary polarization degree in the energy acceptance region;
- it is necessary to have a high intensity photon beam to compensate the reduced energy interval of collected particles and limited efficiency of photon conversion into positrons.

Several target models for the ILC have been proposed. As it has been already pointed out, Titanium and Tungsten targets of different shapes have been widely investigated [28]. Recently, a liquid metal target [29] has been proposed. In this case high Z metals are used, such as Lead (Pb), Bismuth-Lead (Bi-Pb), Mercury (Hg) and In-Ga alloy filled with W powder. With respect to a solid target, a liquid one has several advantages:

a) not accumulate fatigue,

b) easy cooling,

c) compactness.

An interesting example is provided by Mercury: a Hg liquid target has low boiling temperature. This means that, when the absorbed heat brings Hg to the boiling point, the latent vaporization heat comes on scene, which allows absorbing significant amount of heat energy having moderate temperature.

2.2 Polarized photon production

The two most promizing ideas to produce polarized photons at ILC are:

- a high energy (150 GeV) electron beam passing through a helical undulator (see Fig. 2.2);

- Compton scattering of an electron beam (in the GeV energy range) off a CO_2 or Nd:YAG laser (see Fig. 2.3).

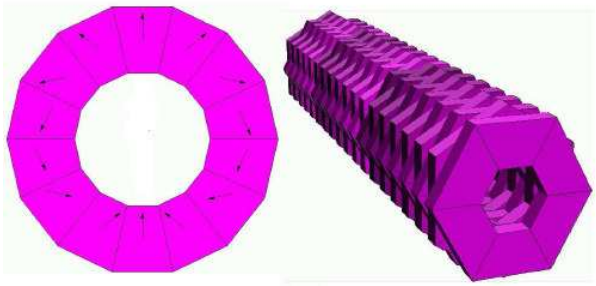

Figure 2.2: Helical undulator scheme. Dipole field created by many permanent-magnets blocks arranged in a ring. Many rings are stacked together and rotated to create the helical field.

The issues associated with target engineering, capture yield optimization and positron polarization are identical for both types of schemes. Generation of circularly polarized photons using lasers or undulators is due to essentially the same physical mechanism. In fact, the polarized photons are due to the helical motion of an electron beam. The only difference is that for the Compton source this motion occurs in a circularly polarized laser wave, while for the undulator in a helical magnetic field. In both schemes a positron polarization of $|P_{e^+}| \geq 60\%$ is expected.

However the two schemes are different under many aspects. For example, the undulator seems technically easier but the laser scheme seems to be more flexible especially for obtaining harder photons and for switching over their helicity.

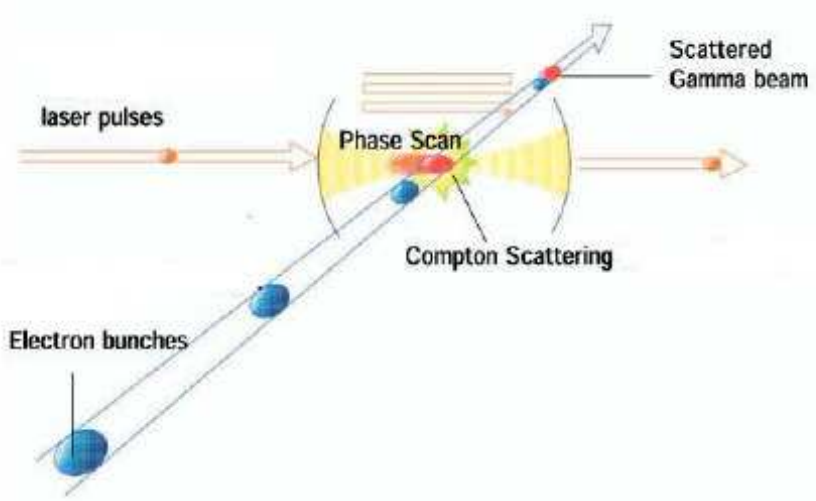

Figure 2.3: Conceptual view of the interaction between the laser and the electron bunches in the Compton scheme.

2.3 Undulator-based polarized positron source

A polarized positron source based on the radiation from an undulator was first proposed by Balakin and Mikhailichenko in 1979 [24].

This method requires a multi-hundred GeV electron beam and, in order to save on ILC cost, it has been proposed to use the beam of the electron main linac. The polarized positron source layout is showed in Fig. 2.4.

The low emittance electron beam is extracted from the electron main linac at an energy of about 150 Gev and transported through ∼200 m of the helical undulator. This is done so that the electron beam energy does not vary if the collision energy is changed. The electrons are deviated by a small bending angle, accelerated through a linac and sent to the interaction point. The photons produced in the undulator are collimated and sent on the thin target to produce positrons. After the target the positron capture system

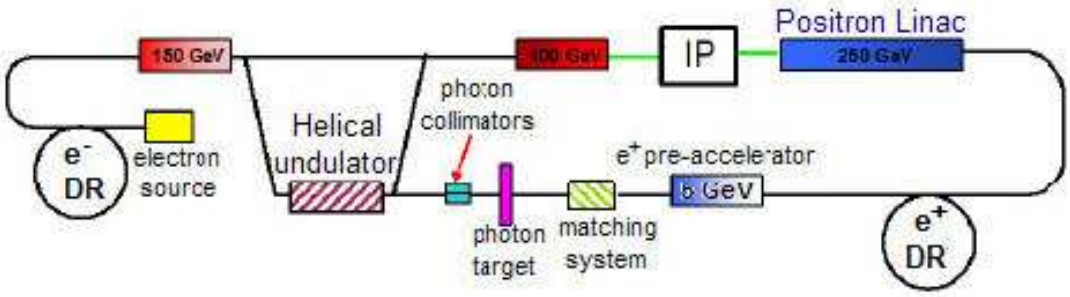

Figure 2.4: ILC essential layout with the undulator scheme for the polarized positron source.

consists of an adiabatic matching device (high field pulsed focusing lens) and a high gradient RF capture section surrounded by a focusing solenoid. Positrons need then to be transported back to the beginning of the linac. Studies [42] have shown that the undulator scheme adds an additional energy spread of 0.15% to the electron beam.

The parameters of the undulator are:

- a magnetic field of 1.1T;
- an undulator period of 1 cm;
- a generated photon energy range of the order of 10 MeV.

The E-166 experiment at SLAC [32] tested either the fundamental process of generating circularly-polarized photons in a helical undulator and the polarized positron production via pair production in a thin target. The electron beam (that had a maximum energy of about 50 GeV and a charge of 10^{10} electrons per bunch) passes through a 1 m long pulsed helical undulator (with a period of 2.54 mm) to generate the circularly polarized photons. The photons were converted to positrons (and electrons) in a thin, moveable target. Titanium and tungsten targets have been tested. The expected values were about $10^6 - 10^7$ positrons (in 15 minutes runs) with an energy up to 10 MeV and beam polarization from about 50% to 80%. A preliminary analysis

of the E166 data agrees well with general expectations but final evaluation of analyzing power and beam polarization is still to be done [25].

2.4 Compton based polarized positron source

The Compton source consists of a storage ring with laser cavities where the Compton interaction between the laser photons and the electron beam provides polarized photons. With such photons it is possible to obtain polarized positrons in the same way as in the undulator method. In contrast to this, the Compton scheme advantages are:

- complete indipendence from the electron main linac. This feature avoids complex interferences between the two main linacs (electrons and positron): this is important especially during the commissioning procedure. Furthermore, it is also important for a good availability of the collider: in fact, if the positron line depends on the electron linac (as in the undulator-based source), when the e^- system is in trouble and during its recovery time, positrons are not available. After the e^- system is recovered, the e^+ system has to be restarted: as a result, an additional time for the e^+ recovery is consumed at every e^- troubles.

- thanks to the independency, there is large flexibility to change the beam structure, intensity, etc. . . , of each linac;

- performances can be improved by introducing some new technology (e.g. more powerful laser system or more precise high-gain optical cavity);

- there is no limitation for low energy operation of ILC. Collisions at the energies from 5 GeV up to 250 GeV can be easily obtained without any cost;

- the positron polarization depends on the laser helicity which can be easily switched pulse by pulse. In the undulator scheme this switching requires an extra section;

- no additional energy spread to the electron beam.

2.4.1 Basics of Compton scattering

The crucial point, in order to estimate the feasibility of Compton ring, is the photon-electron interaction. The variable that governs the Compton scattering is the scaled squared centre of mass energy of the electron-photon system:

$$x = \frac{4E_0\omega_0}{m^2c^4}\cos^2\frac{\alpha}{2} \simeq 0.019\frac{E_0(GeV)}{\lambda(\mu m)} \ ,$$

where E_0 is the electron beam energy, ω_0 is the laser photon energy, λ is the laser wavelength and α ($\sim 8^\circ$, as proposed in [42]) represents the crossing angle between the electron beam and the laser. Using the variable x, the maximum energy of the scattered photons can be written as:

$$E_\gamma < \frac{x}{x+1}E_0 \ .$$

Relevant x values for polarized positron production are small (of the order of 10^{-2}) [42] [5].

Compton scattering has an important property: it conserves parity, then the total and the differential cross sections do not depend on the individual electron (P_e) and laser (λ_C) polarizations but only on their product $P_e\lambda_C$. Fig. 2.5 shows the total cross section as a function of x (left) and the photon energy spectrum for $x = 0.01$, for $P_e\lambda_C = 0$ and $P_e\lambda_C = -1$ (right). The x dependence of the cross section at small x is not relevant and the polarization dependence almost negligible.

Fig. 2.6 shows that the scattered photon polarization dependence on the electron polarization is very small at small x. Hence the laser polarization is the dominant parameter and it is not necessary to have polarized electrons in the storage ring. For a highly polarized laser, the Compton scattering allows to produce high energy photons with a high polarization level.

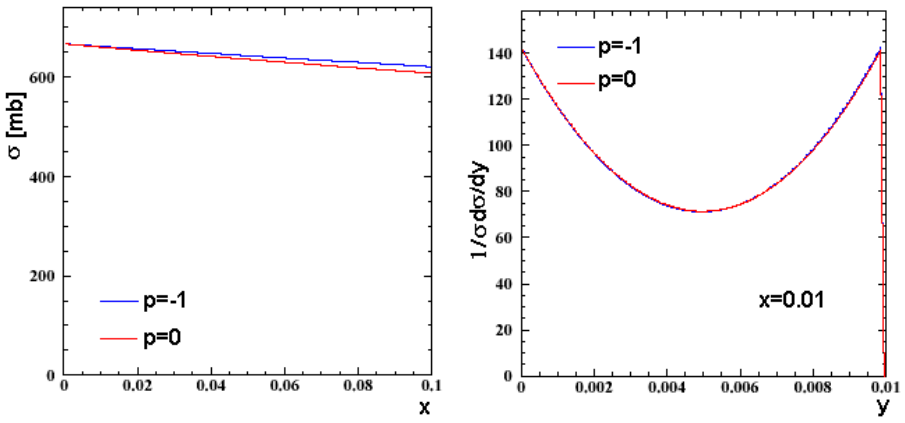

Figure 2.5: Total Compton cross section (left) and photon energy spectrum (right) for different electron/laser polarization. P represents the two polarization product and y is the photon energy normalized at the beam energy.

An important parameter in the photon-electron interaction is the laser photon density (or alternatively the laser field strength). This parameter is related to a nonlinearity parameter that can be defined as [33]:

$$a_0 = \frac{\lambda}{c}\sqrt{\frac{2r_0 I}{\pi mc}} = 0.85 \times 10^{-9}[\lambda(\mu\mathrm{m})][I(\mathrm{W/cm^2})^{1/2}] \ , \qquad (2.1)$$

where r_0 is the classical electron radius and I is the laser intensity. When $a_0 << 1$ only the linear Compton (Thomson) scattering occurs, i.e. only the process $e^-\gamma \rightarrow e^-\gamma$ occurs. On the contrary, when a_0 takes great values a single e^- can scatter simultaneously with two or more laser photons (non linear Compton scattering). In the linear Compton scattering the photons are emitted in a lightly directed beam along the e^- beam direction with a divergence of the order of $1/\gamma$ (γ is the electron relativistic factor) [30]. The energies of the photons produced under non linear interactions are higher than that produced under linear interaction but the emission angular distribution is spread throughout the e^- beam direction [31]. The non linear interaction generates photons that are not easily controllable for the positron

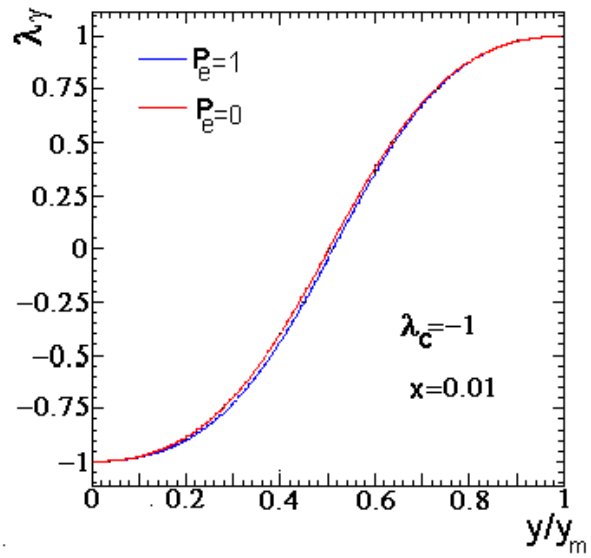

Figure 2.6: Scattered photon polarization as a function of y/y_m, i.e. the ratio between photon energy and its maximum value. Photon polarization is represented for $P_e = 0$ and $P_e = -1$, $x = 0.01$ and λ_C=-1.

production [30]. Therefore, the laser intensity in Compton Ring has to be chosen so that it works in the linear Compton regime ($a_0 \simeq 10^{-2}$).

2.4.2 Snowmass proposal

The first proposal for ILC Compton scheme has been submitted to Snowmass Conference in 2005 [42], where the scientific community has discussed about the physics, the detectors and the accelerator design for the International Linear Collider. In the following the Compton scheme proposed at Snowmass05 will be named 'Snowmass proposal'. Fig. 2.7 shows the complete layout of the proposed Compton source. The electrons are injected in the Compton Ring by an electron linac. The polarized photon production occurs in 30 laser stacking cavities (i.e. optical cavities where laser pulses are stacked) which are installed in a straight section of the Compton Ring. The laser cavities are positioned so to realize a crossing angle between the

electron beam and the laser photons. The produced photons impact on the conversion target and produce the positrons. After the target there is a capture section and a pre-accelerator linac that injects positrons in a damping ring before they are sent to the main positron linac.

Two versions of this design have been taken into account: one uses CO2 laser and the other uses Nd:YAG laser, with a wavelength of 10.6 μm and 1.06 μm, respectively. For identical laser parameters (laser pulse dimensions and photon energy) the CO2 has ten times more photons/pulse than the Nd:YAG; however the Nd:YAG laser can be focused to a significantly smaller spot size. Furthermore the Nd:YAG laser technology is better suited to develop high finesse resonators so improving the photon intensity. Also the Compton ring energy needs to be higher in the CO2 version to obtain the same scattered photon energy.

The proposed ring cirumference for the CO2 design is 649.2 m and the electron beam energy is 4.1 GeV. In the ring two trains of bunches are stored. Each train contains 280 bunches and the bunch-to-bunch spacing is 3.077 ns. For the YAG design (electron beam energy equal to 1.3 GeV) the proposal consists of a 276.7 m circumference and of a train (280 bunches) with the same bunch-to-bunch spacing as in the CO2 design. The bunch population is 6.2×10^{10} electrons for both designs.

Collisions between electrons and laser are the cause of bunch lengthening and can produce a distortion of the longitudinal bunch distributions. Due to this effect, after some turns the amount of the scattered gamma rays becomes practically zero, if laser photons always exist in the cavities. A way to cure this problem, is turning off the laser so that the bunch can turn in the ring without interacting with the photons.

In the YAG ($CO2$) scheme, the laser cavities are filled by photons only in 90 (110) μs which correspond to 100 (50) turns in the Compton ring. Then the laser is turned off in 9.9 ms: in this time electron bunch length becomes shorter and goes back to the primary length thanks to the synchrotron radiation process (see Chapter 5). Each laser stacking cavity stores a photon

bunch whose energy is 210 mJ (600 mJ), and it operates at 100 Hz. The laser pulse duration is 110 μs for CO2 design and 90 μs for YAG design.

In the YAG ($CO2$) scheme, the average number of scattered gamma rays per turn, in the energy range of 23-29 MeV, is expected to be 1.36×10^{10}/bunch (1.8×10^{10}/bunch). The ratio between the produced photons and the positrons obtained by the conversion in the target will be $\sim 1.4\%$. Then the average number of positrons is expected to be 1.9×10^{8}/bunch (2.4×10^{8}/bunch).

The positron pre-accelerator linac accelerates the positrons up to 5 GeV. After acceleration, positrons are sent to the damping ring.

The damping ring circumference is chosen to be 3247 m in CO2 scheme (5 times larger than that of the Compton ring) or 2767 m in YAG scheme (10 times larger than that of the Compton ring). The damping ring stores 10 trains with inter-train gap of 133 ns (CO2 design) or 61 ns (YAG design).

In the Compton scheme the damping ring has two functions: stacking and damping. In fact due to its large circumference, it can store the full number of positron bunches, while at the same time providing a significant damping over the 10 ms repetition period of the laser-beam collisions in the Compton ring. In addition, the longitudinal bucket areas (i.e. stable longitudinal phase space trajectories) of the proposed damping rings is large (due to the small momentum compaction factor and the high RF voltage [36]) which facilitates stacking. Choosing the damping ring for accumulation also avoids the construction of another ring before the damping ring. The damping ring accumulates for 100 ms and then damps for the following 100 ms (close to 10 damping times), for a 5 Hz main-linac repetition rate.

In Table 2.1 the main parameters of the Snowmass proposal Compton rings are summarized.

2.4.3 The ATF experiment

Another advantage of the Compton ring scheme is that its critical elements can be tested before the real construction and partly studied just now. This feature is remarkable in contrast to the undulator scheme: indeed its op-

Parameters	CO2	YAG
Electron energy (GeV)	4.1	1.3
Electron bunch charge (nC)	10	10
RF frequency (MHz)	650	650
Horizontal beam size at IP(μm)	25	25
Vertical beam size at IP(μm)	5	5
Bunch length at IP(mm)	5	5
Laser photon energy (eV)	0.116	1.164
Laser radius at IP(μm)	25	5
Laser pulse width (mm)	0.9	0.9
Laser pulse power/cavity (mJ)	210	592
Number of laser cavities	30	30
Crossing angle (degree)	8	8

Table 2.1: Main parameters of Snowmass proposal Compton rings.

erativity is hard to be demonstrate at reasonable scale before to the construction. An experiment has been made at the KEK-ATF [34] to make a first demonstration of laser-based schemes, and to develop the polarimetry of short pulses of photons and of positrons. In this experiment an electron beam and a Nd:YAG laser are used. At the collision point, that is located in the extraction line of the ATF, a laser cavity is installed. The positions and angles of laser and electron beams are adjusted in order to realize accurate head-on collisions. The polarization of the produced photons is measured by a transmission method [35]. The experiment results have demonstrated for the first time the viability of the Compton ring scheme, in particular it has demonstrated the polarized photon production via Compton scattering, the electron-positron pair creations, and the possibility to collect polarized positrons selecting their energy. Using a circularly polarized laser beam of 532 nm scattered off an electron beam at 1.28 GeV, 10^7/bunch polarized gamma-rays (energy of 56 MeV) were produced and 10^4/bunch polarized positrons were yielded. The measured positron polarization was

$73 \pm 15\%(stat) \pm 19\%(syst)$. This value is in good agreement with $77 \pm 10\%$, that was the result of Monte-Carlo simulations [35], in which basic QED processes and beam parameters were involved. Various techniques developed in this study to find the optimal condition for laser-electron beam collisions will be of great support to design the extremely precise beam diagnostics required by ILC. The ATF results encourage the realization of polarized positron beam for the ILC via Compton source. The next step at KEK-ATF will be to install an optical Compton cavity at the collision point in the storage ring. This will allow to test not only the polarization propagation from laser photons to $\gamma-$rays and then to e^+e^-, but also the bunch dynamics in the Compton ring. This new experiment is scheduled to start in October 2006.

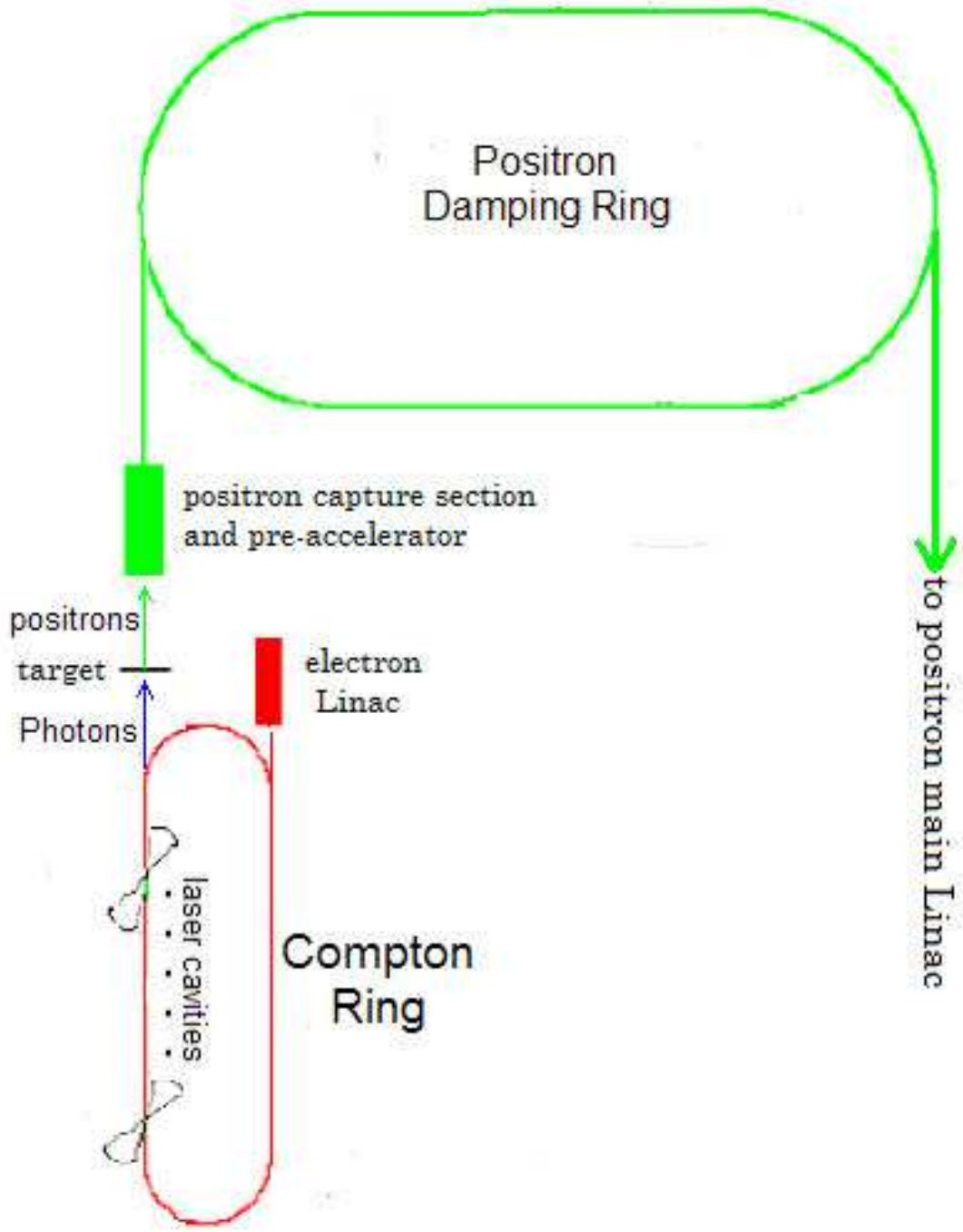

Figure 2.7: Snowmass proposal for the Compton source layout.

Chapter 3

Lattice design for ILC Compton ring

To verify the feasibility of a Compton source for ILC it is necessary to study the Compton interaction effects on the electron beam for different lattice configurations of the Compton Ring (CR). These lattices are expected to satisfy the Snowmass proposal for a Nd:YAG laser scheme, as summarized in Table 2.1.

3.0.4 MAD program

To analyze different lattices the program MAD (Methodical Accelerator Design) [22] has been used. MAD is a tool to study charged-particle optics in alternating-gradient accelerators and beam lines. It can handle from very large to very small accelerators, and it is able to solve different problematics of such machines. This program calculates many beam optics properties, working in a six-dimensional phase space, defined by the set of canonical variables:

$$(x, p_x/p_0)\ , \qquad (y, p_y/p_0)\ , \qquad (-c\Delta t, \Delta E/E_0)$$

where x and y refer to the horizontal and vertical axis, perpendicular to the particle orbit, p_0 and E_0 represent the design momentum and the design

energy respectively, ΔE is the particle energy deviation from the design energy, and Δt is the particle time distance from the synchronous particle.

The ring is represented as a sequence of physical elements, placed around a reference orbit:

1) magnetic elements: dipoles, quadrupoles, sextupoles, etc;

2) non magnetic elements: drift sections, RF cavities, monitors, etc.

The reference orbit consists of a series of straight line segments and circular arcs. It is defined under the assumption that all elements are perfectly aligned.

Each element is characterized by the length and the field strength, which determine the effects on the beam. MAD is used for the calculation of the lattice optics parameters like dispersion, beta-functions, betatron tunes, emittance, ...(see Appendix B), to solve problems like lattice matching or calculation of closed orbits and for particle tracking.

3.1 Lattice choice

3.1.1 Equilibrium emittance

To enlarge the number of photons produced at the interaction point (IP) between the laser and the electron bunch, it is important to have very small transverse bunch dimensions at IP [42]. To minimize the transverse beam sizes one has to design a lattice with a small beam emittance [36].

The beam emittance (and therefore the beam dimension) in an electron storage ring is mainly determined by the synchrotron radiation process, that is characterized by two opposite effects: radiation damping and quantum excitation [37] [38]. The particle beam emittance is given by an equilibrium between the quantum excitation, that causes individual particles to oscillate transversally, and the radiation damping of the betatron oscillations. Taking into account these two phenomena the resulting horizontal equilibrium emittance ϵ_{x_0} (natural emittance) is given by:

$$\epsilon_{x_0} = \frac{C_q \gamma^2 \langle H/\rho^3 \rangle}{J_x \langle 1/\rho^2 \rangle} \tag{3.1}$$

where $\langle\rangle$ means the average value around the ring and

ρ is bending radius,

γ is energy in mc^2 units,

J_x is horizontal damping partition number [41], and C_q is a costant:

$C_q = \frac{55}{32\sqrt{3}} \frac{\hbar}{mc} = 3.84 \cdot 10^{-13}$ m.

In Eq. (3.1) H is the Courant-Snyder dispersion invariant that depends on the guide field properties and is given by:

$$H = \gamma_x D^2 + 2\alpha_x D D' + \beta_x D'^2 \ , \tag{3.2}$$

where D is the dispersion function, D' is the dispersion derivative with respect to the arc length, α_x, β_x and γ_x are the Twiss parameters (see Appendix B).

Eq. (3.1) shows that, for a low emittance lattice design, an important request is to minimize the average H function in the bending magnets.

In a perfect machine the vertical emittance is zero because in the vertical plane there is radiation damping but ideally no dispersion and hence no quantum excitation (in real life a small effect arises due to the fact that the photons are not emitted exactly in the electron direction: anyway the resulting vertical emittance is negligible) [38]. In the real machines the vertical emittance is determined by the coupling between the horizontal and vertical planes due to the imperfections and misalignments of the magnets. This coupling modifies the emittance expressions as:

$$\epsilon_x = \frac{1}{1+\kappa}\epsilon_{x_0} \qquad \epsilon_y = \frac{\kappa}{1+\kappa}\epsilon_{x_0} \tag{3.3}$$

where $\kappa \leq 1$ is the coupling constant [36], ϵ_x and ϵ_y are the effective emittances.

Table 3.1 shows the optics parameters at the interaction point expected to maximize the interaction between the laser and the electron beam.

ϵ_x(m rad)	5×10^{-10}
$\kappa = \epsilon_y/\epsilon_x$	0.02
β_x(m)	1.25
β_y(m)	2.5
$\sigma_x(\mu$m)	25
$\sigma_y(\mu$m)	5

Table 3.1: Optics parameters at the interaction point according to the Snowmass proposal. ϵ_x is the horizontal emittance, k is the coupling constant, β_x and β_y are the betatron functions, σ_x and σ_y are, respectively, the horizontal and vertical bunch dimensions.

3.1.2 Small momentum compaction

The momentum compaction factor α_1 is defined as:

$$\frac{dL}{L} = \alpha_1 \frac{dp}{p} \qquad \alpha_1 = \frac{1}{L}\int \frac{D(s)}{\rho(s)} ds \ ,$$

where L is the particle path along the ring and the integral has to be done along the ring.

In addition to small transverse dimensions, the achievement of a large luminosity between the electrons and the laser photons requires a very small bunch length (∼5 mm) as well. In a storage ring the bunch length can be expressed as:

$$\sigma_L = \frac{\alpha_1 L_0}{2\pi\nu_s} \sigma_{\Delta E/E_0} \ , \tag{3.4}$$

where L_0 is the machine length, $\sigma_{\Delta E/E_0}$ is the energy spread and ν_s is the synchrotron frequency given by:

$$\nu_s = \sqrt{\frac{\alpha_1 c 2\pi\nu_{RF}\sqrt{V_{RF}^2 - U_0^2}}{E_0 L_0}} \tag{3.5}$$

with ν_{RF} the RF frequency, V_{RF} the RF voltage and U_0 the energy radiated by the synchronous particle [36]. Eq. (3.4) shows that the smaller is the momentum compaction α_1, the shorter is the bunch length σ_L.

Furthermore, a very low α_1 is also important because when the electron looses an amount of energy (ΔE), in one quarter of the synchrotron period ($1/(4\nu_s)$), it changes its longitudinal position in the bunch of a quantity:

$$\Delta s = \frac{\alpha_1 L_0}{2\pi\nu_s}\frac{\Delta E}{E} \ . \tag{3.6}$$

As a consequence, if α_1 is not enough low, after few turns, the laser and the electron bunch are no longer synchronous, causing a reduction in luminosity.

As a conclusion, the momentum compaction is a critical parameter for the electron beam interaction with the laser cavity; this explains the importance of designing a lattice that allows enough flexibility in the momentum compaction choice.

3.1.3 Lattice type

The basic structure of a storage ring consists of arc sections and straight sections used for injection, radio frequency (RF), diagnostics and, specifically in the CR, for the laser-e^- interaction region (IR). Each arc section is made up of elementary cells. An important consideration is that the emittance depends only on the arc cell configuration. In particular, in each lattice type, in absence of any wiggler, the minimum emittance value is given by:

$$\epsilon_{x,min} = \frac{F_L(\mu_x)}{12\sqrt{15}} C_q \gamma^2 \frac{\theta^3}{J_x} \ , \tag{3.7}$$

where θ is the dipole bending angle ($\theta = 2\pi/N$, with N the number of cells) and $F_L(\mu_x)$ (the so called 'lattice quality factor') is a function of the betatron phase advance μ_x per cell and strongly depends on the cell lattice style.

Various configurations are possible for the arc cells, e.g.:

1) DFA (Double Focusing Achromat or basic Chasman-Green) [43]

2) FODO (Focusing Defocusing cell) [43]

3) TME (Theoretical Minimum Emittance) [44].

DFA represents the most compact of the structures used in low emittance storage rings. It is very useful in the synchrotron light sources and it is used when one needs a vanishing dispersion in the straight sections. The basic scheme uses two dipole magnets with a focusing quadrupole between them. However the quadrupole does not provide focusing in both planes: this gives severe constraints on the optical function flexibility. Upgrades of this arc cell configuration are the so called expanded Chasman-Green achromat DBA (Double Bend Achromat) and the TBA (Triple Bend Achromat) [43], where defocusing quadrupoles, upstream and downstream the focusing quadrupole, restore focusing in both planes, providing more flexibility.

A FODO lattice consists of an alternating focusing and defocusing quadrupole sequence, separated by bending magnets. Generally this configuration presents a large flexibility in the adjustment of the optical functions.

In preliminary studies to choose the better solution for Compton ring lattice, it has been designed a ring at 1.3 GeV energy (in agreement with the Snowmass request), made up of 96 equal elementary FODO cells and a RF cavity.

Fig. 3.1 reports the horizontal emittance as a function of the phase advance. As the figure shows, to achieve a small emittance, a large phase advance and, hence, a very strong focusing (see Appendix B) are required. The minimum emittance achievable with this configuration is $\sim 4 \times 10^{-9}$ m rad that corresponds to a 'lattice quality factor' of ~ 200. This value can be compared to the theoretical value that can be calculated by Eq. (3.7). In fact, in the case of a FODO lattice, to obtain the minimum emittance, $F_L(\mu_x)$ has to be $\sim$100 [46]. Using this information and approximating $J_x \sim 1$, it is possible to estimate the theoretical minimum horizontal emittance achievable in the lattice with 96 FODO cells: $\epsilon_{x,min} = 1.58 \times 10^{-9}$ m rad. This value is near the minimum emittance that one can read in Fig. 3.1. However, this value is too much large with respect to the Snowmass proposal. One can

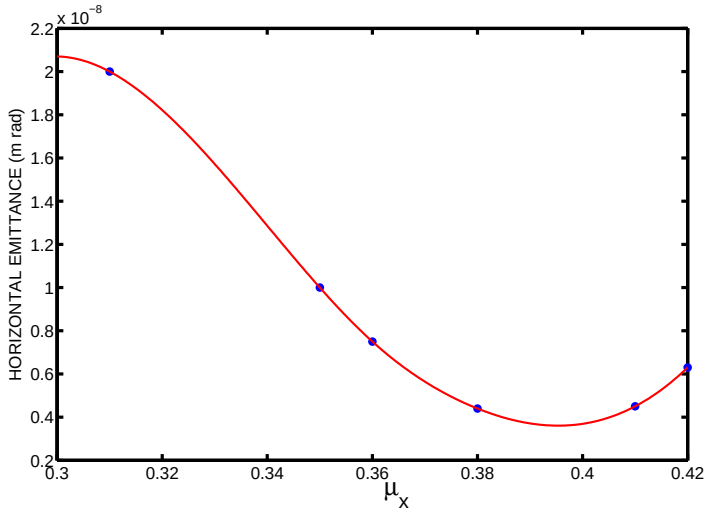

Figure 3.1: Horizontal emittance as a function of the phase advance for a ring with 96 FODO cells.

attempt to improve this result by increasing the number of cells. Increasing the number of cells also reduces the momentum compaction, as it can be seen from Fig. 3.2, where the momentum compaction of a FODO ring is shown as a function of the number of cells. Anyway, to achieve a low momentum compaction and the required emittance, it is needed a large number of cells, and therefore the ring becomes too long.

As a conclusion, FODO is not a good solution for the CR lattice design.

The TME lattice is made up of two half bending magnets (at the beginning and at the end of the cell), and two focusing (F) and two defocusing (D) quadrupoles with the scheme: D-F-F-D. Quadrupoles are separated by drift spaces. The TME lattice is often preferred for a storage ring, because:

- it allows the minimum emittance for a given energy and bending angle, by an accurate adjustment of the optical functions;
- a very low equilibrium emittance is achieved with relatively few arc cells, making the design economic;

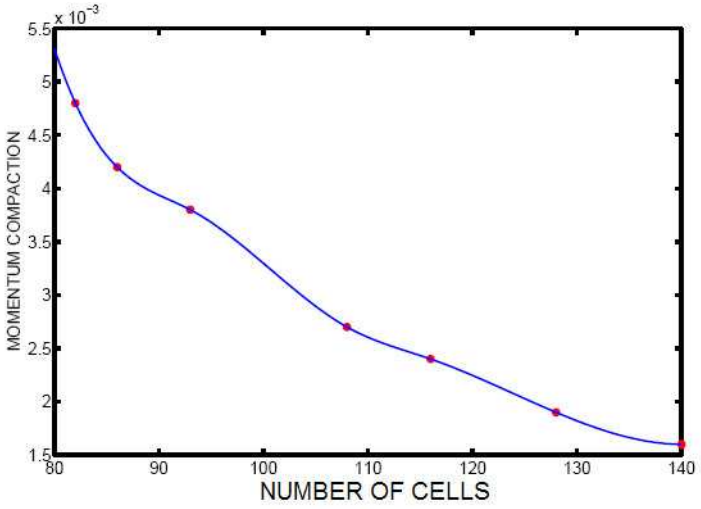

Figure 3.2: Momentum compaction as a function of the number of FODO cells.

- the number of dispersion-free straight sections is relatively small, so there is no need to match the dispersion to zero outside every arc cell (as in a DFA);

- it allows enough flexibility in the momentum compaction choice by changing the phase advance per cell;

- several studies have put in evidence [47] the possibility to achieve a good dynamic aperture.

The TME cell has been adopted for the ILC damping ring (DR) and it is expected to have very good performances. In particular, a good dynamic aperture and a large energy acceptance has been obtained from simulations. Taking into account these considerations, the TME lattice has been adopted also for the CR lattice design.

3.2 Lattice structure

As a first step in the Compton Ring lattice design, a study of the optical functions and machine parameters of a ring based on TME cells has been performed. This study has been done to have a first idea about the possible cell parameters for the Compton Ring, taking into account the machine parameters proposed at Snowmass 2005 (see Table 3.1).

The TME elementary cell (called $ACELL$) is represented in Fig. 3.3. This figure shows:

a) the cell magnetic layout;

b) the horizontal and vertical betatron functions and the dispersion function along the cell.

	$BA2$	$BA2M$	$DLA2$	$DLA3$
$L(m)$	0.25	0.25	0.40	0.40
θ_d(rad)	0.04	0.04		

Table 3.2: Bending magnets lengths (L) and angles (θ_d) and drift space lengths (L) in the elementary cell.

	QFA	QDA
$L(m)$	0.20	0.20
$K1(m^{-2})$	3.52	-3.34

Table 3.3: Quadrupole lengths (L) and quadrupole strengths ($K1$).

The cell parameters are summarized in Table 3.2 and Table 3.3 where:

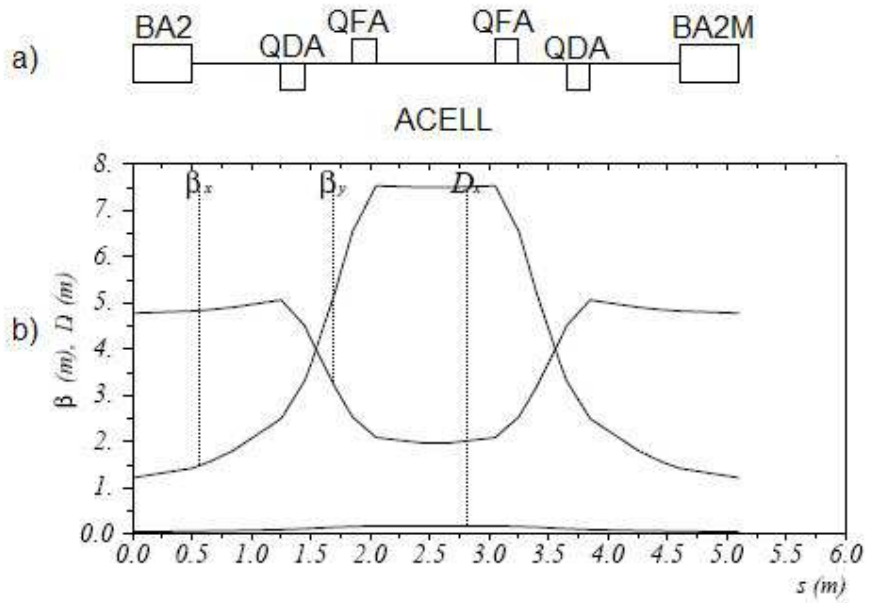

Figure 3.3: a) Magnetic layout of the elementary cell and b) the betatron functions and the dispersion functions.

- $BA2$ and $BA2M$ the are two halves of the bending sectors located at the beginning and at the end of the elementary cell;
- QDA and QFA represent, respectively, the defocusing and the focusing quadrupoles, and $K1$ is the quadrupole strength;
- $DLA2$ and $DLA3$ are the drift spaces separating quadrupoles and bending magnets;
- θ_d is the bending angle.

A RF cavity with a length of 0.2 m has been inserted in one of the arc cells, in the drift space between the two focusing quadrupoles (QFA). The results of the analysis of the quadrupole strengths and quadrupole lengths have provided a starting point for cell dimensions ($\sim$ 5 m, as one can see in Fig. 3.3) and parameters.

To optimize the storage ring length (and therefore the number of cells), the following parameters have to be kept under considerations:

- the horizontal phase advance;
- the horizontal emittance;
- the momentum compaction;
- the chromaticity ξ;
- the focusing and defocusing quadrupoles strengths (KFA and KDA respectively);
- the horizontal dispersion D_x;
- the maximum and minimum value of the horizontal and vertical betatron functions, $\beta_{x,y}max$ and $\beta_{x,y}min$.

First, in order to study the behaviour of these parameters in such a ring, a machine with 78 elementary cells and a RF cavity has been considered. With this number of cells a very low emittance is expected. Fig. 3.4 and Fig. 3.5 report the emittance ϵ_x and the momentum compaction α_c as a function of the horizontal phase advance μ_x, for the 78 cells lattice.

These figures show that, for μ_x greater than 0.4, there are not great variations of the horizontal emittance and momentum compaction trend.

Fig.3.4 shows that the minimum emittance is reached very near to $\mu_x \sim 0.5$ where the cell becomes unstable. The figure shows that the minimum emittance value is:

$$\epsilon_{x,min} = 8.7 \times 10^{-11}\text{m} \cdot \text{rad} \ . \tag{3.8}$$

If one takes into consideration that:

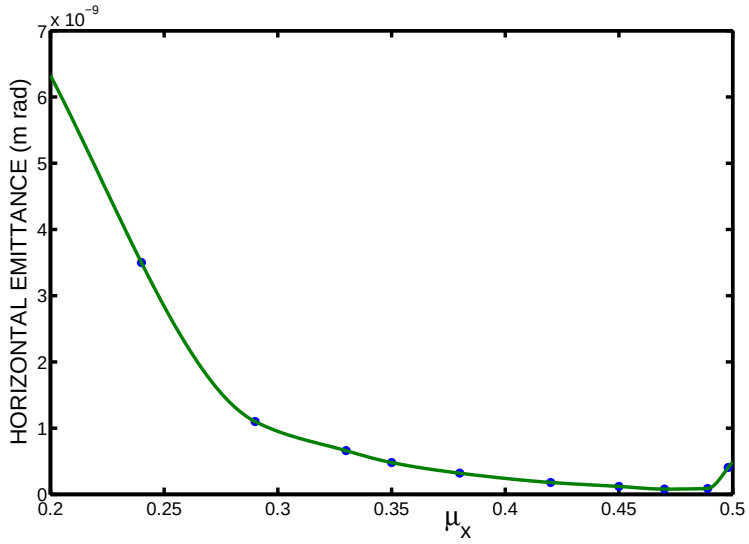

Figure 3.4: The emittance as a function of the phase advance for a ring with 78 cells

- the arc bending angle θ with 78 cells is (N is the number of cells):

$$\theta = \frac{2\pi}{N} = 0.08\text{rad} \ ;$$

- the electron energy is 1.3 GeV;
- $J_x \sim 1$ (the value is obtained by the MAD output);

one can calculate (using Eq. 3.7 and the minimum emittance reported in Eq. 3.8) that the 'lattice quality factor' is $F_L(\mu_x) \sim 3$.

A TME lattice with 78 cells would satisfy the Compton Ring emittance requirement for a value of μ_x larger than 0.45. As it has already pointed out previously, a large value of μ_x (near to 0.5) needs a strong focusing, which leads to unacceptable dynamical behaviour. Therefore it is necessary to check the quadrupole strength for different phase advances. Fig. 3.6 shows the focusing quadrupole strength as a function of μ_x in a lattice with 78 cells: $\mu_x < 0.4$ results to be a good solution in order to have an acceptable focusing (defocusing) quadrupole strength value.

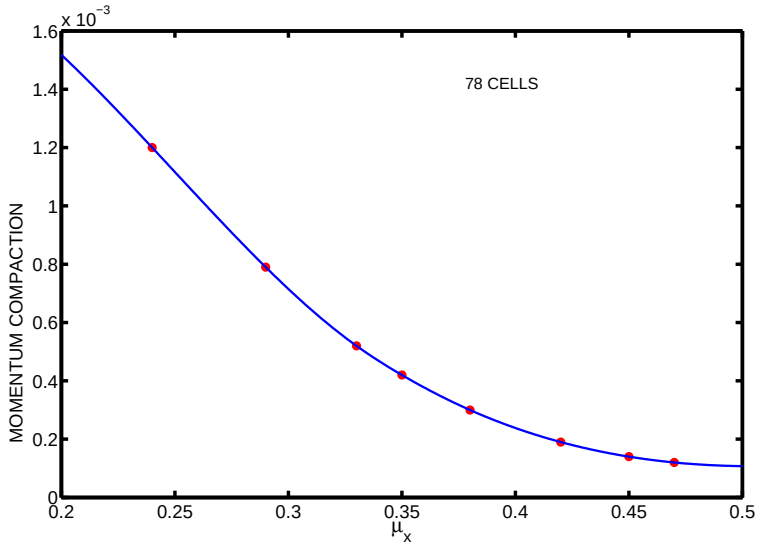

Figure 3.5: Momentum compaction as a function of the phase advance in a ring with 78 cells

The horizontal emittance behaviour as a function of the quadrupole strength is shown in Fig.3.7 for the 78 cells lattice: in order to obtain a very low value of the horizontal emittance, a high value of the quadrupole strength is necessary.

But, a too strong quadrupole strength implies a too large natural chromaticity: Fig.3.8 shows the horizontal chromaticity behaviour as a function of the horizontal emittance. A very small emittance requires a very large chromaticity. The drawback of a large chromaticity is that a lot of sextupoles are necessary in order to correct it. But, sextupoles give non-linear effects in the machine that affect the beam stability and reduce the dynamic aperture.

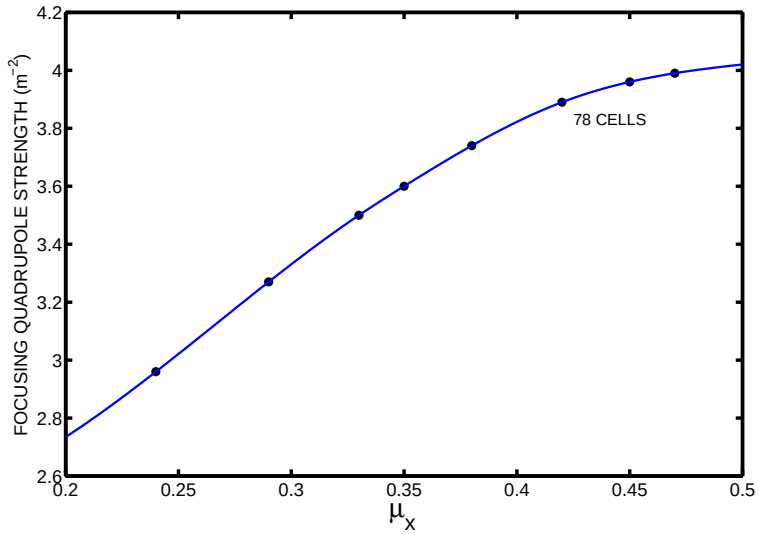

Figure 3.6: Quadrupole strength as a function of μ_x in a lattice with 78 cells.

Looking at the expression of $\epsilon_{x,min}$ (Eq. (3.7)) it is clear that, to have a very small emittance, one has to divide the lattice in a number of cells as large as possible. On the contrary, the reduction of the number of cells helps to reduce the machine cost.

Further tests have been done to study the emittance and the momentum compaction variations with respect to the number of cells.

Rings with 96, 90, 78, 76, 68, 60 cells have been considered so to have a ring circumference near the Snowmass requests.

Fig. 3.10 and Fig. 3.11 report the horizontal emittance and the momentum compaction as a function of the number of cells.

In the same figures the number of cells fulfilling to the Snowmass values are shown for the horizontal emittance and the momentum compaction. The

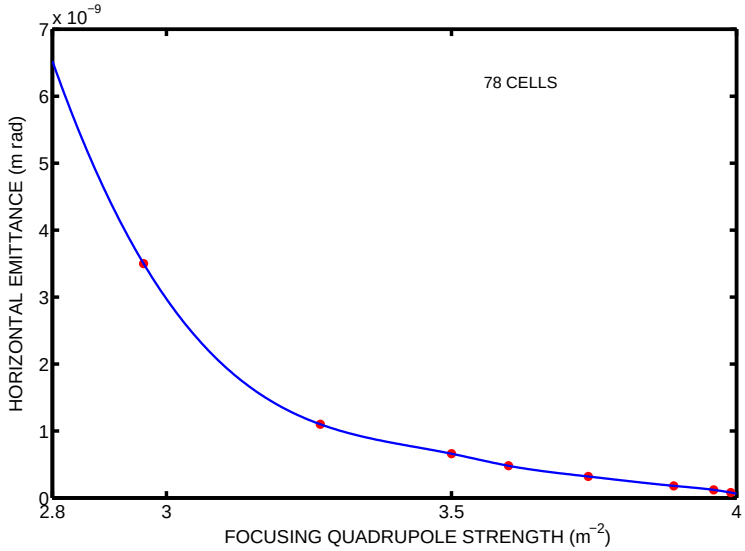

Figure 3.7: The emittance as a function of the focusing quadrupole strength in the case of a lattice with 78 cells.

Snowmass parameters can be obtained with 80-90 cells, that corresponds to a Compton ring circumference of $\sim$ 400 m. The following chapter will be devoted to study how to reduce the ring circumference mantaining the emittance and the momentum compaction near the Snowmass requests.

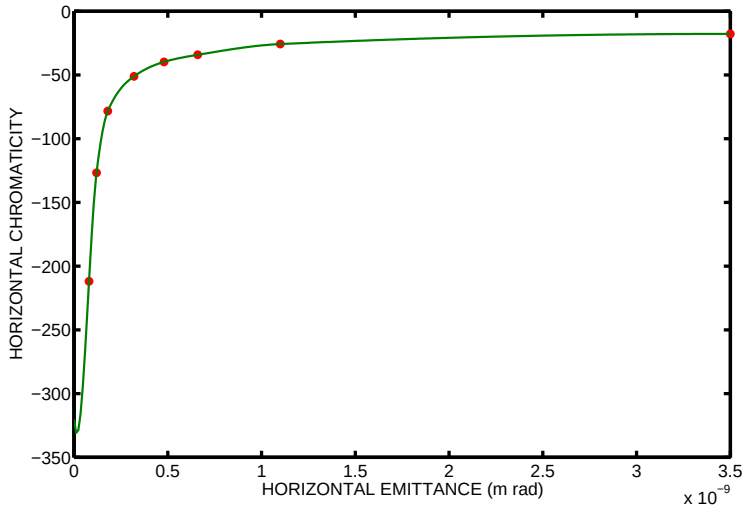

Figure 3.8: Horizontal chromaticity as a function of the emittance in a ring with 78 cells

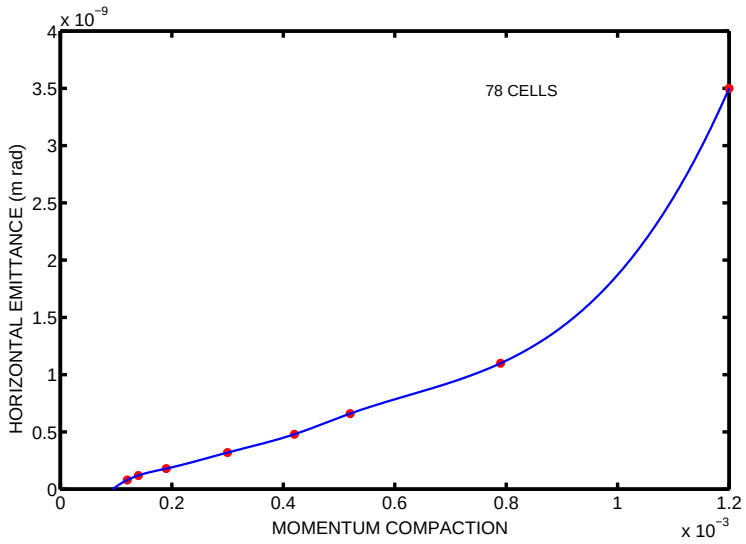

Figure 3.9: Horizontal emittance as a function of the momentum compaction for a lattice with 78 cells

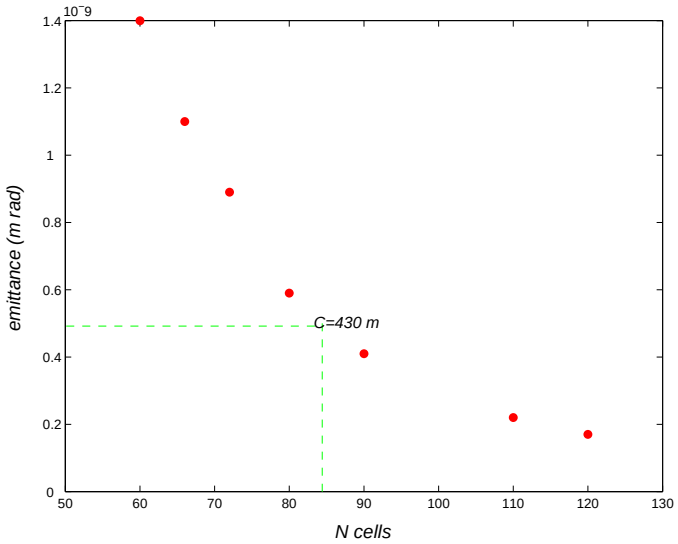

Figure 3.10: Horizontal emittance as a function of the number of cells. C represents the circumference value for a ring with 84 cells.

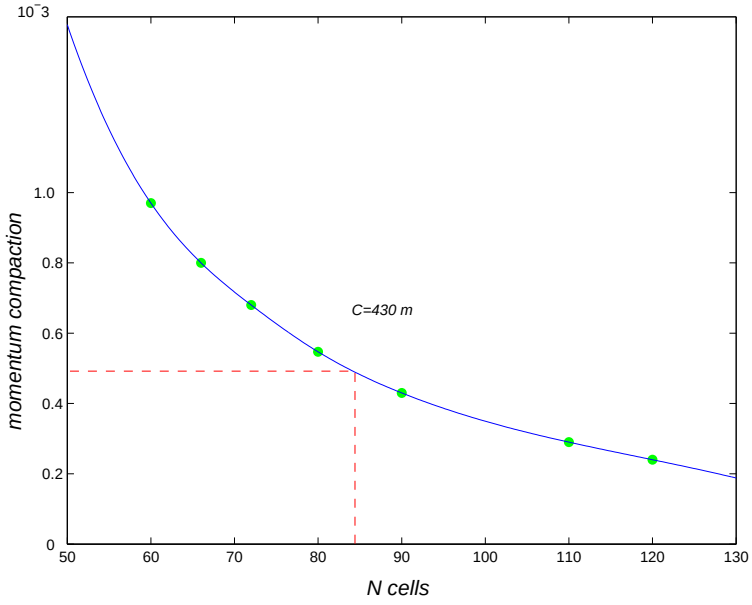

Figure 3.11: Momentum compaction as a function of the number of cells.

Chapter 4

Transverse dynamics

4.1 Dispersion suppressor

The performances of a low emittance lattice can be improved using insertion devices. However, to obtain the requested effect, it is necessary to handle the dispersion function where one wants to put the insertion devices. For example, if one inserts some wigglers in a lattice, the emittance can decrease or increase if they are put in a region where dispersion is low or high, respectively (see Appendix C). This explains why a dispersion suppressor (called $SUPCELL$) has been added to the ring structure presented in the previous section in order to set to zero the dispersion in two straight sections of the ring.

The dispersion suppressor cell has the same structure of the elementary cell ($ACELL$); the only differences are the strengths of two quadrupoles, named QFM and QDM, and the length of the drift space between QDM and the dipole at the end of the cell, where the dispersion and its derivative are set to zero (the magnetic layout of $SUPCELL$ is shown in Fig. 4.2). The lengths (L) and strengths ($K1$) of the focusing (QFM) and defocusing (QDM) quadrupole, calculated using the MAD program, are shown in Table 4.1. Comparing the values of this table to the ones reported in Table 3.3 one can note that the new quadrupoles (QFM and QDM) have the same length of QFA and QDA and that their focusing and defocusing strength

	QFM	QDM
$L(m)$	0.20	0.20
$K1(\mathrm{m}^{-2})$	3.91	-4.27

Table 4.1: Focusing (QFM) and defocusing (QDM) quadrupole lengths (L) and strengths ($K1$).

(respectively) is bigger than that of the elementary cell quadrupoles.

4.2 Wiggler properties

A wiggler is a magnetic device [45] consisting of a dipole sequence with alternating polarity, arranged so that there is no net beam deflection or displacement. There are several reasons for installing wigglers in an electron ring. In the synchrotron light sources they are installed to take advantage of the peculiar characteristics of their radiation with respect to that emitted by the bending magnets:

- Higher photon energies. The radiation energy emitted by the wiggler depends on the magnetic field strength, which can be greater than the one of the ring bending magnets;
- Increased photon flux. Using many emitting poles the total photon flux increases proportionally;
- Increased brightness (photon flux per unit area and solid angle) and quasi-monochromatic spectrum.

In machines like colliders, damping rings or like the CR under consideration, wigglers are used to increase the radiation damping and to modify various beam parameters as damping time, bunch length, energy spread and emittance (see Appendix C).

There are different wiggler types. The dipole wiggler, proposed to be used in the Compton Ring lattice and called *damping wiggler*, gives rise mainly to changes in equilibrium emittance, energy spread and damping times.

A second use of wigglers is to control electron spin polarization. Due to the synchrotron radiation emission, electrons tend to become polarized with their spins aligned in the vertical direction. Therefore, wigglers can be used to increase the polarization level. The wigglers inserted in the ILC Compton Ring lattice are such that this phenomenon is negligible, since the polarization time is very long; anyway the polarization of the electron beam is not required.

If the energy loss in the ring is completely dominated by the wiggler the natural emittance is given by [46]:

$$\epsilon_w \simeq \frac{8}{15\pi} C_q (\frac{e}{mc})^3 \langle \beta_x \rangle \frac{\mid B \mid^3}{\gamma k_w^2} \ , \tag{4.1}$$

where $\langle \beta_x \rangle$ is the mean beta function in the wiggler, B represents the wiggler peak magnetic field and k_w is the wiggler wave number.

When both arcs and wigglers contribute to the energy loss, the equilibrium emittance can be written as [46]:

$$\epsilon_{tot} = \epsilon_{arc} \frac{J_{x,arc}}{J_{x,arc} + F_w} + \epsilon_{wig} \frac{F_w}{J_{x,arc} + F_w} \ , \tag{4.2}$$

where ϵ_{arc}, $J_{x,arc}$ are the natural emittance and the damping partition number in absence of wigglers respectively. $F_w = \frac{I_{2,wig}}{I_{2,arc}}$ is the ratio of the energy loss in the wiggler over the energy loss in the arcs, where $I_{2,wig}$ and $I_{2,arc}$ are the synchrotron radiation integrals in the arcs and in the wigglers (see Appendix C).

The cell (called $CWIG$), that has been used to add wigglers in the Compton Ring lattice, is made up of two defocusing quadrupoles, two focusing quadrupoles and two wigglers in the straight sections. Each quadrupole has a length of 0.25 m. The $CWIG$ magnetic structure and betatron functions along the cell are shown in Fig.4.1. In the figure, the dispersion function is not reported because it is set at zero in the wiggler section by the presence of the dispersion suppressor.

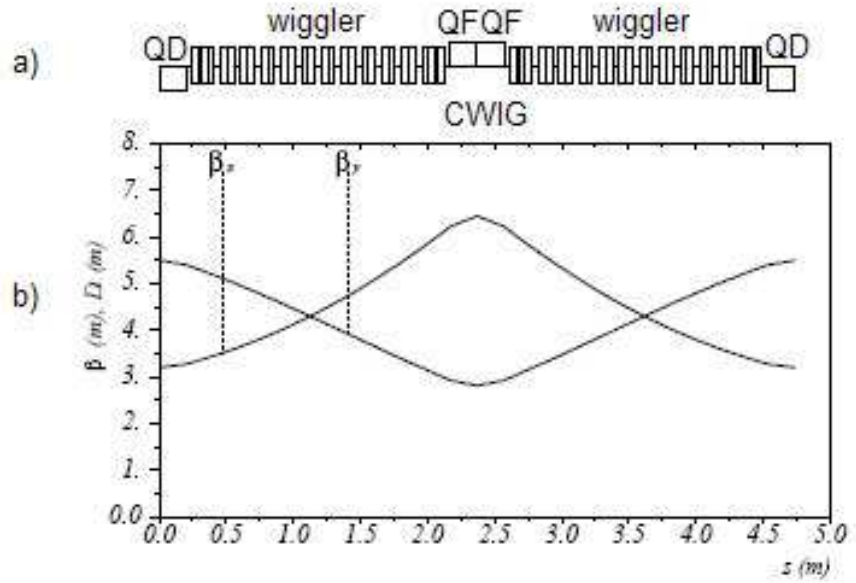

Figure 4.1: a) Magnetic layout of the wiggler section. QF and QD are the focusing and the defocusing quadrupoles respectively. b) Betatron functions in the wiggler section. The dispersion function is zero.

The wiggler parameters used in the Compton Ring lattice are:

- a longitudinal period of 0.4 m;
- a peak field of 1.6 T.

A comparison between the performances of lattices with and without wigglers has been done using the lattice based on TME cells described in the previous chapter; in this case the ring is made up of 60 cells.

The use of several $CWIG$ cells has allowed to reduce the emittance of about a factor two.

To explain this result, it may be useful to write the horizontal emittance (in absence of any wigglers) as:

$$\epsilon_{arc} = C_q \gamma^2 \frac{I_{5,arc}}{J_x I_{2,arc}} \ , \tag{4.3}$$

where $I_{5,arc}$ is the synchrotron radiation integral I_5, defined in Appendix C, in absence of wigglers. In the lattice configurations without wigglers presented in the previous chapter, i.e. with $E_0 = 1.3$ GeV, $I_{5,arc} = 6.87 \times 10^{-4}$ m^{-1} and $I_{2,arc} = 1.31$ m^{-1} (the synchrotron integral values are given by MAD output), Eq. 4.3 gives the emittance:

$$\epsilon_{arc} = 1.3 \times 10^{-9} \mathrm{m} \cdot \mathrm{rad} \ .$$

If one adds twelve $CWIG$ sections in this configuration, the emittance can be calculated using Eq. (4.2). To evaluate wiggler contribution, one can calculate the emittance due to the radiation in the wigglers:

$$\epsilon_w = C_q \gamma^2 \frac{I_{5,w}}{J_x I_{2,w}} \ ,$$

that, with twelve $CWIG$ sections, gives as a result:

$$\epsilon_w \simeq 2.25 \times 10^{-10} m \cdot rad \ .$$

Hence $\epsilon_w \ll \epsilon_{arc}$; furthermore $F_w \gg 1$ and then, as one can see in Eq. (4.2), the lattice emittance is dominated by the wiggler contribution.

4.3 Ring layout

By taking into account all the issues previously discussed, the final ring layout has been designed. The lattice is made up of two arcs and two straight sections. Each arc is made up of TME-like cells and one of them contains the RF cavity. In each straight section there are two interaction regions. The straight sections are symmetric with respect to the center, and in each half straight section there are, in the order, the following sections:

- a dispersion suppressor;

- a matching section made up of five quadrupoles with alternating polarities;
- the interaction region ($IRCELL$);
- 12 wiggler sections ($CWIG$).

The location of the dispersion suppressor before the interaction region allows to set at zero the dispersion function in the interaction region. Having a zero dispersion in the interaction region is important because in this case the bunch horizontal dimension is given by:

$$\sigma_x = \sqrt{\epsilon_x \beta_x + D_x \frac{\Delta p}{p}} \ , \tag{4.4}$$

and therefore, $D_x = 0$ is a needed condition to have a small bunch (a small bunch is important for a high luminosity between the laser and the electrons, as pointed out in Section 3.1). In Fig. 4.2 the beta functions and the dispersion function are shown in the dispersion suppressor and in the interaction region. One can note that, at the interaction point, β_x and β_y are fixed to 1.5 m and 2.5 m respectively (in agreement with the values proposed at Snowmass05): these values are sufficiently low to ensure small transverse dimensions σ_x and σ_y ($\sigma_y = \sqrt{\epsilon_y \beta_y}$). After the interaction region the dispersion function is still zero. Therefore, having the wigglers after the interaction region, ensures to have the dispersion function equal to zero inside them.

The MAD program has been used to calculate the lattice of straight section in order to satisfy all the requirements on the optical functions and to match the optical functions of the straight section to the arcs. In particular the quadrupoles of the wiggler cell have been calculated in order to obtain the value of the average β_x needed to get the desired emittance. The quadrupoles of the matching section and of the interaction region have been used to achieve the desired values of β_x, β_y at the IP, to match the optical functions

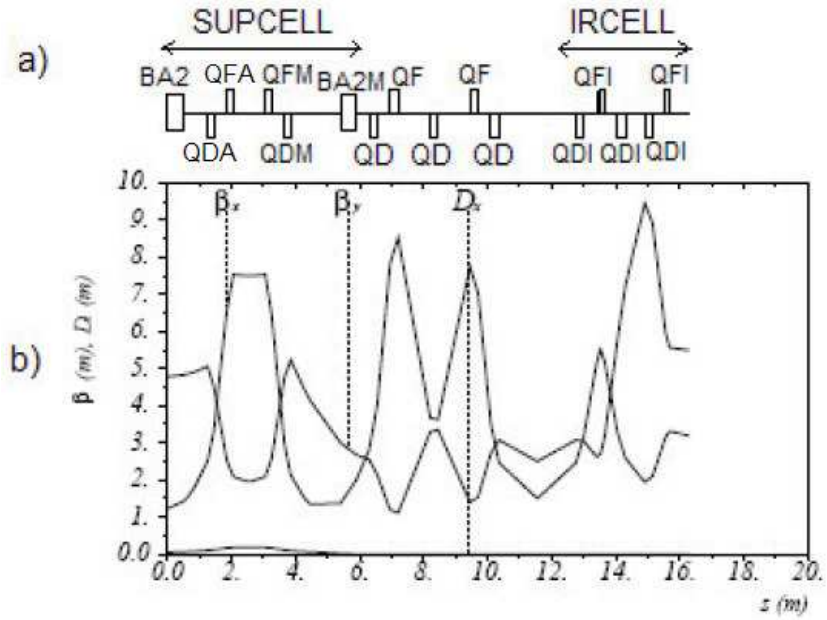

Figure 4.2: a) Magnetic layout of the dispersion suppressor, of the interaction region and of the quadrupoles between them. QFM, QFI and QF are focusing quadrupoles, QDM, QDI and QD are defocusing quadrupoles. b)The betatron functions and the dispersion function in the section.

of the arc to those of the wiggler and to adjust the betatron tunes of the ring. The results of the matching procedure applied to the different sections of the Compton Ring lattice are shown in Fig. 4.3. The figure shows the behaviour of the betatron functions and of the dispersion function along a quarter of ring from the center of the arc to the center of the straight section (14 elementary cells, a dispersion suppressor, an interaction region and three wiggler sections). Both the center of the arc and the center of the straight section are symmetry points of the ring.

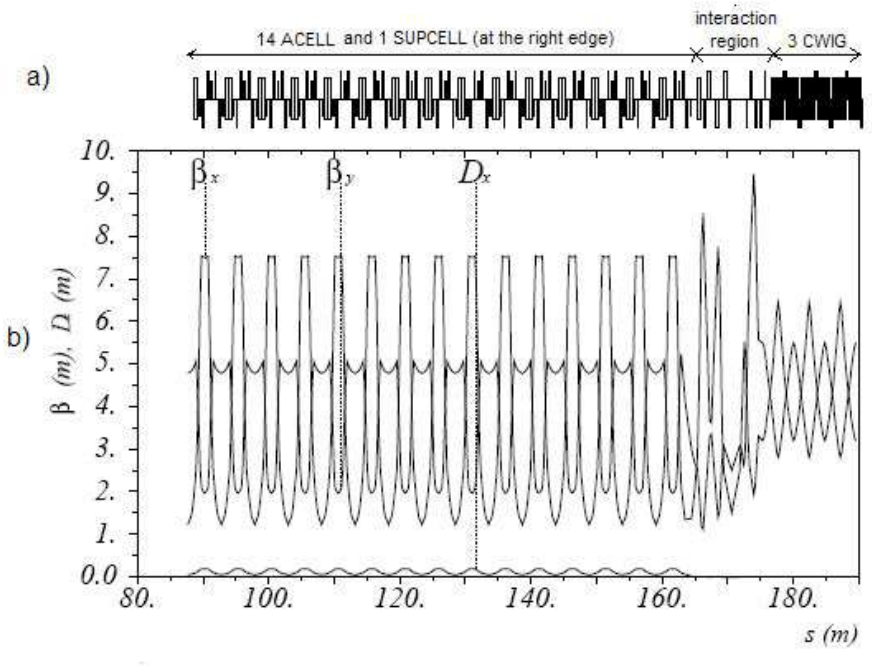

Figure 4.3: a) Magnetic layout of a quarter of the ring. b) Betatron functions and dispersion function.

4.4 Lattice studies

Table 4.2 shows four different lattice configurations (A, B, C and D).

The four configurations differ in the beam energy, in the bunch dimensions and in wigglers.

In Table 4.2 the value K represents the root square of the coupling constant (κ) defined in Table 3.1; in the same table the transverse dimensions and the betatron functions are referred to the interaction region (IR) and the harmonic number H is defined as:

$$H = \frac{\nu_{RF}}{\nu_0} \ , \tag{4.5}$$

where ν_{RF} is the RF frequency and ν_0 is the bunch revolution frequency. Table 4.2 distinguishes the parameters in input and output parameters.

Having fixed σ_y, β_x and β_y, the σ_x and κ values have been calculated in the different configurations using the following expressions:

$$\sigma_x = \sqrt{\frac{\epsilon_{x_0}}{1+\kappa}\beta_x} \qquad \sigma_y = \sqrt{\frac{\kappa}{1+\kappa}\epsilon_{x_0}\beta_y} \tag{4.6}$$

where ϵ_{x_0} is the natural emittance defined in Eq. (3.1). The bunch vertical dimension has been fixed to 5 and 25 μm: $\sigma_y = 5$ μm is the value proposed at Snowmass05 (see Table 2.1), while $\sigma_y = 25$ μm has been chosen to improve the $Touschek\ life-time$ (see the following section).

The RF frequency and the RF voltage have been set in the different configurations so to maintain the bunch length $\sigma_s \sim$5 mm (see Eq. (3.4)).

One can see in Table 4.2 that the best result (in terms of the horizontal emittance) has been obtained for a lattice with 12 wigglers and with the nominal energy $E_0 = 1.3$ GeV (C lattice): comparing the ϵ_x values for the different configurations one notes that the emittance is reduced by a factor greater than two by the wiggler insertion.

In Table 4.2, σ_{buck} is a parameter that gives informations about the energy acceptance of the RF system. It is defined as the half-height bucket (the bucket indicates the stable trajectories in the longitudinal phase space [36]) in units of the energy spread. The table shows that σ_{buck} is almost the same in all the configurations.

4.5 Touschek life-time

Table 4.2 reports for each configuration the $Touschek\ life-time$ (τ_T).

The Touschek life-time is very sensitive to lattice parameters. For example, it is sensitive to the bunch length: τ_T increases with the bunch length (see Appendix A), and hence it is sensitive to the RF voltage (the bunch length decreases if the RF voltage increases, as one can see in Eq. (3.4)). In Table 4.2 one can see that the best result for τ_T is given by the ring without wigglers and with an increased energy ($E_0 = 1.6$ GeV). However, in this configuration, the horizontal emittance is too high. Therefore it is necessary to design a lattice configuration, where a small emittance is reached with

a reasonable Touschek life-time. To reach this goal, other simulations have been done at different electron beam energies, using, as a starting point, the C configuration of Table 4.2. The results of these studies are reported in Table 4.3 where three configurations have been taken into account (A', B' and C').

Table 4.3 shows that increasing the number of wiggler sections from 12 (A' and B' lattices) to 24 (C' lattice), it has been obtained a larger Touschek lifetime with the same emittance. On the other hand, adding more wigglers is not convenient since it increases the length and the cost of the ring. Therefore, as an optimal solution, a lattice with 12 wiggler sections has been chosen.

The RF voltage has been chosen to achieved a bunch length $\sigma_s \simeq 5$ mm, as for the previous lattices. As one can see in Table 4.3, increasing the energy, the horizontal emittance and the Touscheck life-time increases and ϵ_x maintains the value near to the Snowmass request. Hence, it is possible to conclude that an increasing beam energy from 1.3 GeV to 1.8 or 2.0 GeV allows to increase the Touscheck life-time.

4.6 Chromaticity correction

In a ring design, it is important to correct the natural chromaticity (i.e. the chromaticity induced by quadrupoles [48]) introducing sextupoles at nonzero dispersion positions of the lattice. The chromaticity is a problem for two reasons. First, particles with significant energy deviations may experience a shift of the betatron tunes (the betatron tunes are the number of horizontal and vertical betatron periods per turn, see Appendix B). This 'tune shift' puts them on an integer resonance, where they will not be dynamically stable [48]. Second, some collective phenomena (notably the head-tail instability [53]) are sensitive to the chromaticity, and zero or slightly positive chromaticity is needed to minimize the adverse effects.

The choice of the best sextupole position in the elementary cell permits to correct the chromaticity with the smaller sextupole strength, so avoid-

ing strong non-linear effects that can affect the beam stability (and could eventually require the octupole insertion).

Generally, two sextupole families are needed to correct horizontal and vertical chromaticities. Hence, in the Compton Ring lattice, two types of sextupoles have been used: SF (focusing sextupole, corrects the horizontal chromaticity) and SD (defocusing sextupole, corrects the vertical chromaticity).

In a storage ring the total chromaticity is given by the equation:

$$\xi_{x,tot} = \xi_{x,Q} + \xi_{x,S} \qquad \xi_{y,tot} = \xi_{y,Q} + \xi_{y,S} \tag{4.7}$$

where ξ_Q is the chromaticity contribution from quadrupoles and ξ_S is the contribution from sextupoles. The principles to decide sextupole positions are:

- to locate the chromatic sextupoles near quadrupoles (where $\beta_x D_x$ and $\beta_y D_x$ are maximum), to minimize sextupoles strength;
- to choose a large β_x/β_y ratio for the focusing sextupole and a large β_y/β_x ratio for the defocusing sextupole for optimal indipendent chromaticity control.

Using these guide-lines two sextupole configurations are possible for the lattices of Tables 4.2 and 4.3. These two magnetic configurations (called respectively configuration $S1$ and configuration $S2$) are shown in Figs. 4.4 and 4.5.

Figs. 4.4 and 4.5 show that, in both the sextupolar configurations, a focusing sextupole has been inserted in the elementary cell, in correspondence to the dispersion function maximum value and to the maximum value of the ratio β_x/β_y. The configurations are different with respect to the position of

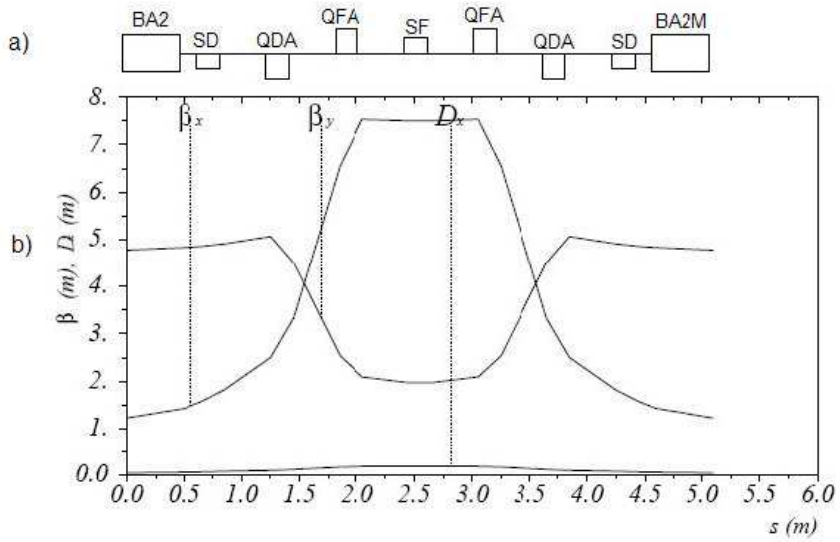

Figure 4.4: Sextupolar configuration $S1$ in the elementary cell. SF and SD are the focusing and the defocusing sextupoles respectively.

the two defocusing sextupoles. Using the chromaticity definition [48], it is possible to rewrite Eq. (4.7) as:

$$\begin{cases} \xi_{x,tot} = -\frac{1}{4\pi}\int \beta_x[K(s) - S(s)D_x(s)]ds \\ \xi_{y,tot} = \frac{1}{4\pi}\int \beta_y[K(s) - S(s)D_x(s)]ds \ , \end{cases} \tag{4.8}$$

where $S(s)$ is the sextupole strength and $K(s)$ represents the quadrupole strengths. The total chromaticities can be written as a function of the focusing and defocusing sextupole strengths (S_D and S_F):

$$\begin{cases} \xi_{x,tot} = \xi_{x,Q} + \tilde{A}S_F + \tilde{C}S_D \\ \xi_{y,tot} = \xi_{y,Q} - \tilde{B}S_F - \tilde{D}S_D \end{cases} \tag{4.9}$$

where the variables $\tilde{A}$, $\tilde{B}$, $\tilde{C}$ and $\tilde{D}$ have been introduced:

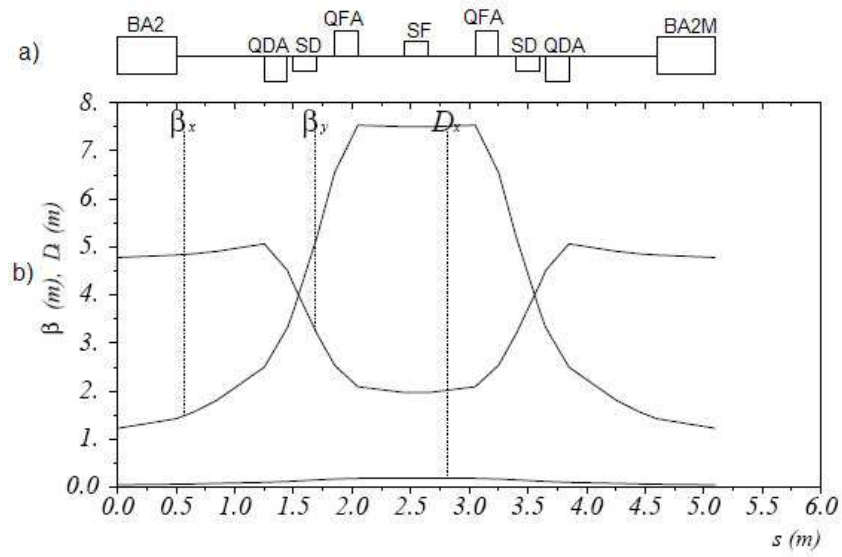

Figure 4.5: Sextupolar configuration $S2$ in the elementary cell. SF and SD are the focusing and the defocusing sextupoles respectively.

$$\begin{cases} \tilde{A} = \frac{1}{4\pi}\int_{SF}\beta_x D_x \\ \tilde{B} = \frac{1}{4\pi}\int_{SF}\beta_y D_x \\ \tilde{C} = \frac{1}{4\pi}\int_{SD}\beta_x D_x \\ \tilde{D} = \frac{1}{4\pi}\int_{SD}\beta_y D_x \ , \end{cases}$$

where the integrals in $\tilde{A}$ and $\tilde{B}$ expressions are calculated in the focusing sextupoles and the integrals in $\tilde{C}$ and $\tilde{D}$ expressions are calculated in the defocusing sextupoles.

After the evaluation of the natural chromaticities ($\xi_{(x,y),Q}$) and of the variables $\tilde{A}$, $\tilde{B}$, $\tilde{C}$ and $\tilde{D}$ of Eq. (4.9), the sextupole strengths (S_F and S_D), needed to correct the chromaticities along the ring, have been obtained. Table 4.4 shows the natural chromaticities and the sextupole strengths obtained in the two sextupolar configurations.

One can conclude, according to these results (shown in Table 4.4), that the best configuration to correct the chromaticity is the configuration $S1$ (Fig.4.4) because it is possible to set $\xi_{x,tot}$ and $\xi_{y,tot} \sim 0$ with a lower sextupole

strength.

4.7 Dynamic aperture

The dynamic aperture is the innermost region in the phase space, where the motion is stable. Trajectories with initial conditions in this domain remain confined for ever. A large dynamic aperture is an important characteristic for a storage ring. For example, it is necessary to ensure good injection efficiency or to avoid strong limitation for the Touschek life-time [46].

To achieve a good dynamic aperture, one needs to keep the sextupole strengths low. Therefore, the efforts presented in the previous section to minimize the sextupole strengths have been done also to improve the dynamic aperture.

The dynamic aperture has been studied for a lattice with 12 wigglers, a nominal beam energy of 2 GeV (see B' lattice of Table 4.3) and with the sextupolar configuration of Fig. 4.4. As a first step in the search for a ring with a good dynamic aperture, it is necessary to fix accurately the phase advance μ_x. The choice of the best phase advance value can be done studying the transverse phase space contour. This contour has been produced by MAD program, taking a set of particles and tracking the particle phase space coordinates over some number of turns. Fig. 4.6 shows the horizontal phase space for $\mu_x = 0.375$ and for the energy spread $\Delta p/p = 0\%$. In the figure, the most external trajectory is the stable trajectory with the larger phase space coordinates: for $(x, p_x/p_0)$ values external to this trajectory the orbits are unstable. It has been tested that, for $\mu_x < 0.375$, the most external trajectories of Fig. 4.6 are not stable.

Fig. 4.7 reports the relation between the energy spread value and the maximal x coordinate of a stable particle trajectory. One can note that, for an energy spread of 2%, the horizontal dynamic aperture becomes zero.

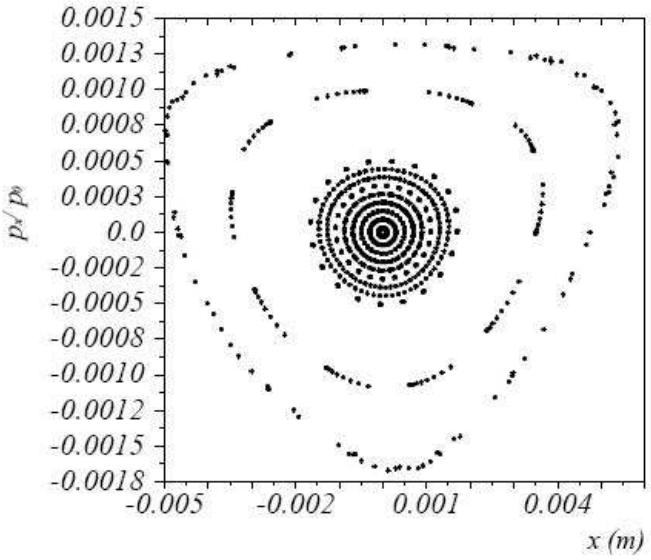

Figure 4.6: The figure represents the particle phase space for the ring configuration B' shown in Table 4.3. The y axis reports p_x/p_0, i.e. the particle horizontal divergence. Particles with an initial value of the trajectory x ¿ 0.0045 m are lost.

Figs. 4.8 and 4.9 show the horizontal and vertical tune values, respectively, as a function of the energy spread. These are important parameters that indicate if the ring is working near a resonance [49]. The figures show that with an energy spread up to 4% the working point is far from any resonance.

Fig. 4.10 reports the maximum initial values of stable trajectories in the (x, y) coordinate space for different energy spread values.

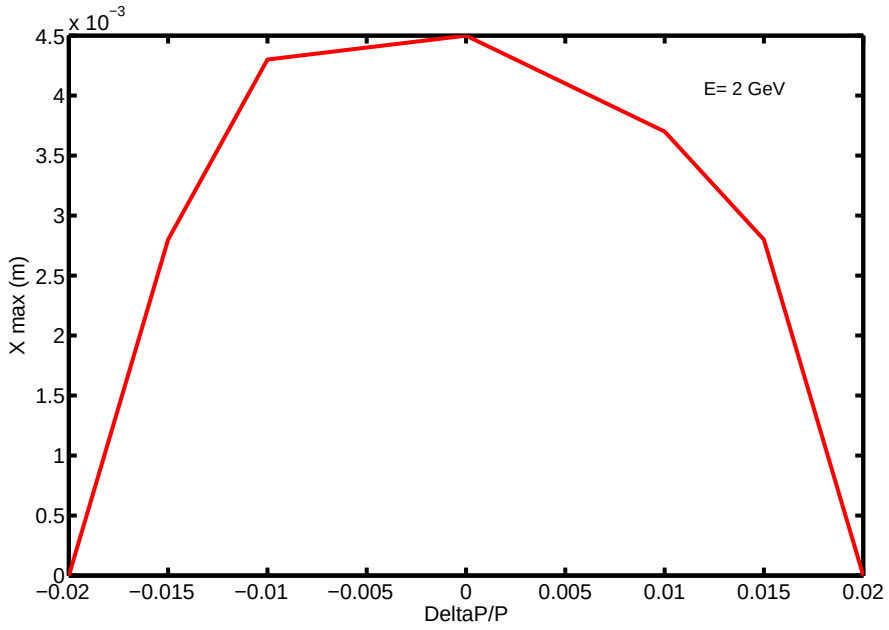

Figure 4.7: Horizontal dynamic aperture dimension at different energy spread values.

As a conclusion one can say that the parameters of the Compton Ring are very challenging for the low emittance and the high bunch density required. In order to satisfy this requirements the insertion of wigglers in the lattice is necessary. In fact the insertion of wigglers allow to reduce the emittance while keeping a reasonable value of the number of cells and of the cell phase advance in the arcs. Moreover it has been shown that the insertion of wigglers allows to increase the Touschek beam lifetime, which is very critical due to the high bunch density. Another way to increase the Touschek lifetime is to increase the beam energy. Both this solutions (insertion of wigglers and increase of the energy with respect to the value of 1.3 GeV proposed at Snowmass) have been used for the B' configuration (see Table 4.3) that has been adopted for our studies.

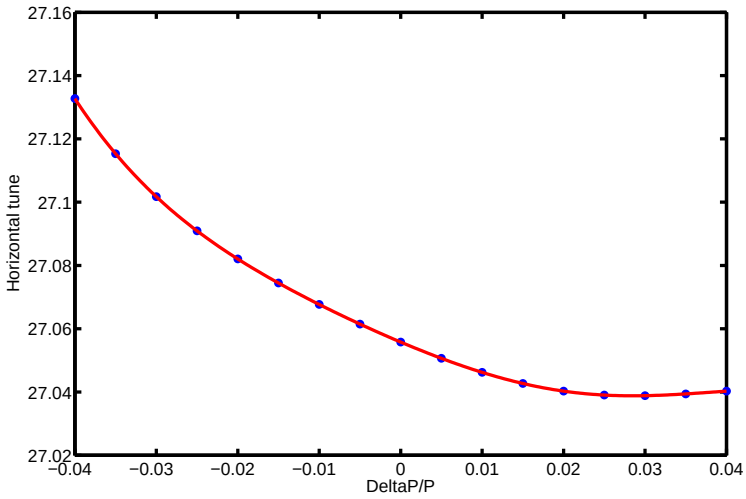

Figure 4.8: Horizontal tune as a function of the energy spread.

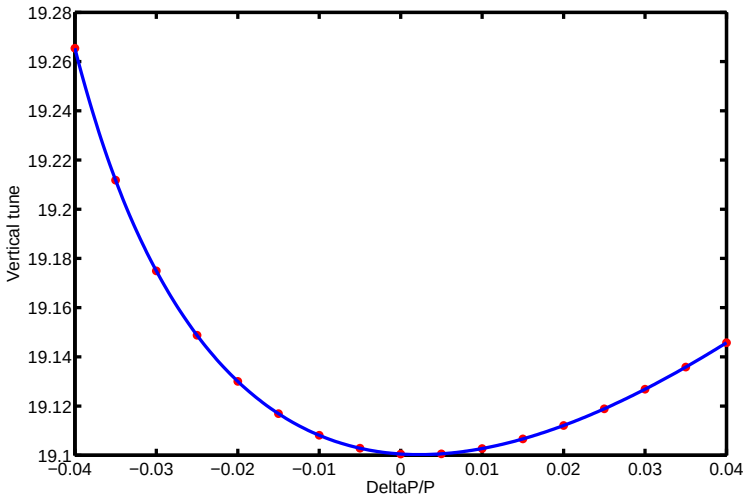

Figure 4.9: Vertical tune as a function of the energy spread.

configuration	A	B	C	D
INPUT PARAMETERS				
β_x(m)	1.5	1.5	1.5	1.5
β_y(m)	2.5	2.5	2.5	2.5
$\sigma_y(\mu$m)	5	25	25	25
Number of particles/bunch	6.2×10^{10}	6.2×10^{10}	6.2×10^{10}	6.2×10^{10}
E_0(GeV)	1.3	1.3	1.3	1.6
Wiggler sections	*no*	*no*	12	*no*
$C(m)$	345	345	408	345
RF Voltage (MV)	0.35	0.35	0.7	0.28
RF frequency (MHz)	500	500	500	500
H	575	575	680	575
OUTPUT PARAMETERS				
σ_s(mm)	5.08	5.08	4.97	4.98
$\sigma_x(\mu$m)	44	40	19	51
$\sigma_x\sigma_y(\mu m^2)$	220	1000	475	1275
α_c	8.07×10^{-4}	8.07×10^{-4}	7.93×10^{-4}	8.07×10^{-4}
Touschek life-time (min)	0.79	3.7	4.6	12.1
K	0.008	0.237	0.980	0.144
σ_{buck}	1.70×10^{-2}	1.70×10^{-2}	1.95×10^{-2}	2.00×10^{-2}
emittance(m rad)	1.3×10^{-9}	1.3×10^{-9}	5.0×10^{-10}	2.0×10^{-9}

Table 4.2: Lattice performances with different configurations.

configuration	A'	B'	C'
INPUT PARAMETERS			
β_x(m)	1.5	1.5	1.5
β_y(m)	2.5	2.5	2.5
$\sigma_y(\mu$m)	25	25	25
Number of particles/bunch	6.2×10^{10}	6.2×10^{10}	6.2×10^{10}
E_0(GeV)	1.8	2.0	1.8
Wiggler sections	12	12	24
$C(m)$	407	407	464
RF Voltage (MV)	1.32	1.60	1.63
RF frequency (MHz)	500	500	500
H	678	678	773
OUTPUT PARAMETERS			
σ_s(mm)	4.95	4.99	5.1
$\sigma_x(\mu$m)	25	28	26
$\sigma_x\sigma_y(\mu m^2)$	625	700	650
α_c	8×10^{-4}	8×10^{-4}	7×10^{-4}
Touschek life-time (min)	12	16.3	54
K	0.78	0.70	0.78
σ_{buck}	2.16×10^{-2}	2.19×10^{-2}	2.13×10^{-2}
$emittance$(m rad)	6.60×10^{-10}	7.61×10^{-10}	6.56×10^{-10}

Table 4.3: The table shows the result simulations made with MAD. In all the lattice configurations the wiggler sections have been put.

	configuration $S1$	configuration $S2$
$\xi_{x,Q}$	-36.11	-36.11
$\xi_{y,Q}$	-22.57	-22.57
$SD(\mathrm{m})^{-3}$	-49.87	-47.83
$SF(\mathrm{m})^{-3}$	36.71	70.46

Table 4.4: Natural chromaticities $\xi_{(x,y),Q}$ and sextupole strengths SD and SF to correct the chromaticities in the two configurations.

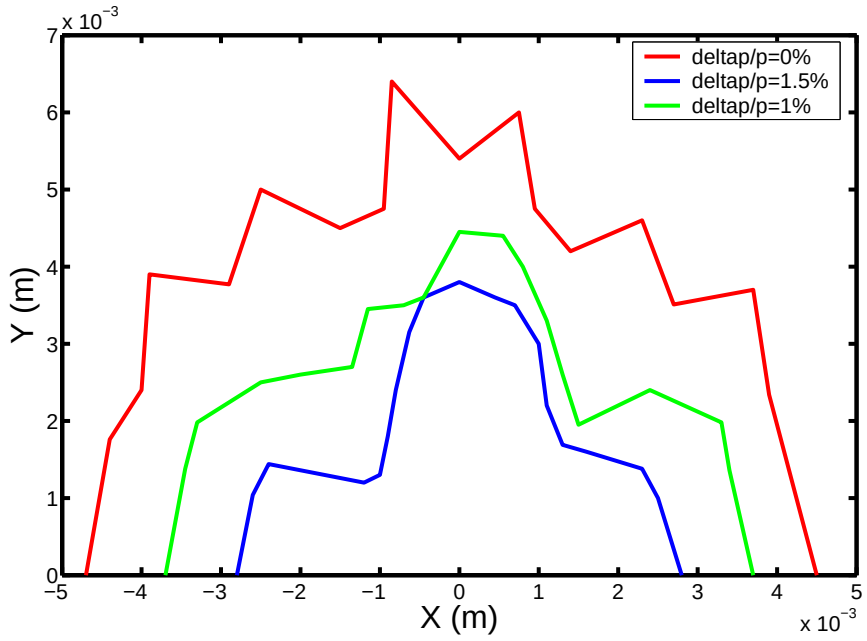

Figure 4.10: Dynamic aperture for an electron beam energy E_0 =2 GeV. Some different energy spreads have been considered.

Chapter 5

Longitudinal single bunch dynamics

In the previous chapters the lattice design for ILC Compton Ring has been discussed. Installing laser cavities in these lattices, the Compton scattering (between the electrons and the laser photons) produces circularly polarized photons. Following the scheme of the Compton source (see Chapter 2), these photons can impact off a target to produce the polarized positrons for the ILC positron beam.

Due to the energy loss in the laser cavities, the single bunch longitudinal dynamics is a critical point in the studies for Compton Rings [42]. To perform longitudinal beam dynamics calculations in the Compton Ring, a dedicated C simulation program has been written. As input parameters for this simulation program, it is possible to use the parameters of the lattices presented in Chapters 3 and 4. In particular one reports the results of the simulations with the lattice C (see Table 4.2), whose parameters are very near to the Snowmass proposal, and with the lattice B' (see Table 4.3) where the energy is 2 GeV (the energy proposed at Snowmass is 1.3 GeV) that presents the best performances, as it has been pointed out in the previous chapter.

5.1 Input and output parameters

To analyse the beam behaviour when circulating in the Compton Ring, the simulation program needs the following input parameters, that depend on the Compton Ring lattice:

- the terms of the momentum compaction linear and non-linear;
- the RF voltage and the harmonic number;
- the synchrotron radiation integrals I_2, I_3 and I_4;
- the ring length;
- the electron number in the bunch and the nominal energy;
- the electron bunch and the laser pulse tranverse dimensions and the laser longitudinal dimension;
- the photon energy and the amount of photons in the laser pulse;
- the crossing angle between the cavity laser and the ring.

Another input parameter is the number of turns that the bunch has to do in the ring. Generally, it is chosen so that the particles turn in the lattice for some damping times. Furthermore, as it has been explained in Chapter 2, one expects that the number of turns, in which the laser is turned on, is a critical point for the beam stability. For this reason, in addition to the total number of turns along the ring, it is necessary to specify as input how many turns the laser is turned on.

To study the bunch stability in the ring, the program gives, as output, the longitudinal phase space and the bunch longitudinal distributions. Furthermore, the program allows also to calculate, for each turn, the number of scattered photons and their spectrum. This allows to understand the efficiency of the Compton Ring in the production of polarized photons for the Compton source goals.

5.2 Macro-particle model

The program analyses beam dynamics in time domain, by simulating several turns of the particles of a bunch along the Compton Ring. In the CR lattice, the electron number in a single bunch is $N_e \sim 10^{10}$, therefore, if one wants to study the bunch time evolution, one has to work with 10^{10} equations. However, this is a too much large number for the computational limits of the modern computers. Rather than to follow the evolution of all the particles, only a limited number of 'macro-particles', ($N_{macro} << N_e$) is taken into account. The macro-particle number must be chosen so that physical information is not lost. Convergence tests (as it will be shown later) have shown that 10^5 macro-particles describe very well the Compton Ring bunch dynamics.

Each macro-particle behaviour in the longitudinal phase space is described by the following canonically conjugated coordinates:

$$P = \frac{E - E_0}{E_0} \qquad \Phi = 2\pi \frac{H}{L_0} z \ , \tag{5.1}$$

where E_0 represents the synchronous particle nominal energy, E is the energy of the macro-particle under study, H is the RF cavity harmonic number, L_0 is the ring length and z is the macro-particle displacement from the synchronous particle ($z > 0$ if the macro-particle is in the head). Hence P is the macro-particle normalized energy spread and Φ is its phase.

The physical effects that have been considered in order to study the single bunch dynamics are the following:

- the synchrotron radiation;
- the RF cavity;
- the interaction between the bunch and the laser;
- the correlation between Φ and P through the momentum compaction (phase advancement).

Considering only the synchrotron radiation, the RF cavity and the phase advancement the longitudinal distributions of the bunch are Gaussian [36]. Therefore, for convergence reasons, at the first turn, one imposes that the initial P and Φ distributions are Gaussian. Under the interaction with the laser, one expects that instabilities affect beam dynamics and the bunch distributions are no longer Gaussian.

5.3 Synchrotron radiation

Each electron emits synchrotron radiation and the energy loss can be written as [36]:

$$U(P) = U_0 + DP \ , \tag{5.2}$$

where U_0 is the energy radiated by the synchronous particle and D is the damping factor defined as:

$$D = \frac{\partial U(P)}{\partial P}|_{P=0} \ . \tag{5.3}$$

U_0 and D are calculated by the program, using the synchrotron radiation integrals and the following relationships [41]:

$$U_0(MeV) = 8.85 \times 10^{-14} E_0(MeV)^4 \frac{I_2}{2\pi} \tag{5.4}$$

$$D = 8.85 \times 10^{-14} E_0(MeV)^4 \frac{2I_2 + I_4}{2\pi} \ , \tag{5.5}$$

where I_2 and I_4 are the synchrotron radiation integrals (defined in Appendix C). Eq. (5.2) is responsible for the radiation damping effect [37]; because of this effect the particle longitudinal phase space spirals, towards the fixed point representing the synchronous particle (see Fig. 5.1). Really the synchrotron radiation phenomenon is a quantum effect, because it consists in the emission of photons that are discret units whose energy and emission time vary randomly. Hence, Eq. (5.2) represents the average value of the energy emitted.

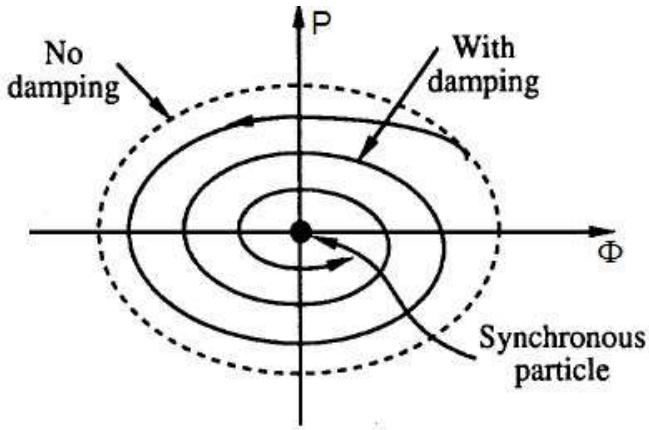

Figure 5.1: Radiation damping effect on the particle longitudinal trajectory.

To take into account the quantum nature of the radiation phenomenon, a new term has to be added in Eq. (5.2); this term can be derived by calculating the energy loss standard deviation, σ_U. The electron energy loss is the combination of two indipendent effects: the probability to emit photons with energy u, and the Poissonian probability to emit N photons. The standard deviation of the energy loss can be derived from these considerations, obtaining [36]:

$$\sigma_U^2 = \langle u^2 \rangle \langle N \rangle \ , \tag{5.6}$$

where $\langle u^2 \rangle$ is the average value of the square power of the emitted photon energy and $\langle N \rangle$ represents the average value of the number of emitted photons on a turn. The previous equation can be written as [38]:

$$\sigma_U^2 = 2D\sigma_E^2 \ , \tag{5.7}$$

where σ_E is the natural energy spread and it can be written as a function of the synchrotron radiation integrals I_2, I_3 and I_4 [41] (see Appendix C):

$$\sigma_E(MeV) = 1.2506 \times 10^{-6} E_0(MeV)^2 \sqrt{\frac{I_3}{2I_2 + I_4}} \ . \tag{5.8}$$

This new term is responsible for the so called quantum excitation effect: the randomness of the emission introduces a sort of noise, causing the oscillation amplitude growth of the longitudinal phase space coordinates.

The opposite effects of radiation damping and quantum excitation lead to Gaussian equilibrium bunch distributions with respect to P and Φ [38]. Therefore, taking into account the radiation damping and the quantum excitation, the synchrotron radiation changes the normalized energy spread of each macro-particle according to:

$$P_{fin} = P_{in} - DP_{in} - \frac{U_0}{E_0} + \frac{1}{E_0}(G\sqrt{2D\sigma_E^2}) \ , \tag{5.9}$$

where P_{fin} and P_{in} represent respectively the energy spread after and before the emission, and G is a random number that obeys to a Gaussian function with standard deviation equal to one and average value equal to zero. The factor G is necessary to take into account that the energy deviation distribution function is Gaussian.

5.4 Phase advancement

The path length L of each particle along a storage ring depends on its energy, according to the following relationship [39]:

$$\frac{L - L_0}{L_0} = \int \sqrt{(1 + \frac{\Delta x}{\rho})^2 + (\frac{d\Delta x}{ds})^2} ds \ , \tag{5.10}$$

where $\Delta x = D(s)P$, $\rho(s)$ is the local radius of curvature and s is the longitudinal coordinate.

Generally, in a storage ring, the term $(\frac{d\Delta x}{ds})^2$ can be neglected and Eq. (5.10) can be written using the momentum compaction [40]:

$$\frac{L - L_0}{L_0} = \alpha_c P \ . \tag{5.11}$$

On the contrary, in the Compton Ring lattice, because of the small momentum compaction lattice and because of the large energy spread induced by the interaction with the laser, it is necessary to consider not only the momentum compaction linear effects but the nonlinear ones as well. By taking into account the dependence of ΔL by P, P^2 and P^3 [39], after one turn, the phase of every macro-particle advances according to:

$$\Phi_{fin} = \Phi_{in} - K_1 P_{in} - K_2 P_{in}^2 - K_3 P_{in}^3 \ , \tag{5.12}$$

where

$$K_1 = 2\pi H \alpha_1 \ , \tag{5.13}$$

$$K_2 = 2\pi H (\alpha_1 + \alpha_2) \ , \tag{5.14}$$

$$K_3 = 2\pi H (\alpha_1 + \alpha_2 + \alpha_3) \ , \tag{5.15}$$

and α_1, α_2 and α_3 are respectively the linear, quadratic and cubic terms of the momentum compaction.

5.5 RF cavity

In the RF cavity every macro-particle gains a part of the energy lost during the turn. When a macro-particle enters the RF cavity, its normalized energy spread, P_{in}, becomes P_{fin} according to:

$$P_{fin} = P_{in} + \frac{eV}{E_0} \cos(\phi_s - \Phi) \ , \tag{5.16}$$

where e is the electron charge, V is the voltage in the RF cavity, ϕ_s is the synchronous phase that is defined so that the synchronous particle gains all the energy lost (U_0) because of synchrotron radiation. Therefore, the synchronous phase is defined as:

$$\phi_s = \pm \arccos(\frac{U_0}{V}) \ , \tag{5.17}$$

where U_0 has been defined in Eq. (5.4) and the sign has to be the same as the one of the momentum compaction in order to have stable synchrotron oscillations [38].

5.6 Interaction with the laser

In the laser cavity, as it has been explained in Chapter 2, the electrons interact with the photons under linear Compton scattering ($e^- + \gamma \longrightarrow e^- + \gamma$). To calculate the laser effects on the electron longitudinal distribution, the first step has been the evaluation of the number of interactions between an electron bunch and a laser pulse.

5.6.1 Number of interactions

The total number of photons, that are produced by the interaction between the bunch and the laser can be derived as:

$$N_I = L \cdot \sigma_C \ , \tag{5.18}$$

where N_I is the number of interactions between the bunch and the laser (that is equal to the number of the produced photons), L is the luminosity of the process and σ_C is the the linear Compton scattering cross section in the laboratory frame.

To calculate L, the starting point has been the formula of the luminosity between two crossing bunches given by [50]:

$$L = 2N_e N_\gamma \cos^2\theta \int\int\int\int \mathrm{d}x\mathrm{d}y\mathrm{d}s\mathrm{d}ct \rho_{e,x}(x_1)\rho_{L,x}(x_2) \cdot \rho_{e,y}(y)\rho_{L,y}(y)\rho_{e,s}(s_1 - ct)\rho_{L,s}(s_2 + ct) \ , \tag{5.19}$$

where θ is half the crossing angle between the laser and the electron bunch, $\rho_{e,x}$ represents the horizontal electron distribution, $\rho_{L,x}$ is the horizontal photon distribution, $\rho_{e,y}$ and $\rho_{L,y}$ are respectively the vertical electron and photon distributions and $\rho_{e,s}$ and $\rho_{L,s}$ are the electron and laser longitudinal distributions. $\rho_{e,x}$, $\rho_{e,y}$, $\rho_{L,x}$ and $\rho_{L,y}$ are expected to be Gaussian with standard deviation, respectively, $\sigma_{L,x}$, $\sigma_{L,y}$, $\sigma_{e,x}$ and $\sigma_{e,y}$:

$$\rho_{L,i} = \frac{\exp[-\frac{x^2}{2\sigma_{L,i}^2}]}{\sqrt{2\pi}\sigma_{L,i}}$$
$$\rho_{e,i} = \frac{\exp[-\frac{x^2}{2\sigma_{e,i}^2}]}{\sqrt{2\pi}\sigma_{e,i}} \ , \tag{5.20}$$

with $i = x, y$.

Also $\rho_{L,s}$ is Gaussian (with standard deviation $\sigma_{L,s}$), while the electron longitudinal distribution, $\rho_{e,s}$, has to be calculated by the program turn by turn: the interaction with the laser causes a distortion of the longitudinal bunch distribution, so that $\rho_{e,s}$ is not Gaussian.

In Eq. (5.19) the crossing angle effect is taken into account by the factor $2\cos^2\theta$ and by performing a variable change relating the coordinates x and s and the new coordinates x_1, x_2, s_1 and s_2:

$$\begin{aligned} x_1 &= -s\sin\theta + x\cos\theta \\ x_2 &= s\sin\theta + x\cos\theta \\ s_1 &= s\cos\theta + x\sin\theta \\ s_2 &= s\cos\theta - x\sin\theta \end{aligned} \tag{5.21}$$

One can note that in Eq. (5.19) it is possible to integrate with respect to the y variable, obtaining:

$$\int \mathrm{d}y \frac{\exp[-\frac{y^2}{2\sigma_{e,y}^2}]}{\sqrt{2\pi}\sigma_{e,y}} \frac{\exp[-\frac{y^2}{2\sigma_{L,y}^2}]}{\sqrt{2\pi}\sigma_{L,y}} = \frac{1}{\sqrt{2\pi}\sqrt{\sigma_{L,y}^2 + \sigma_{e,y}^2}}$$

Substituting x and s in Eq. (5.19) with x_1, x_2 and s_2, one obtains:

$$L = \frac{2N_e N_\gamma \cos^2\theta}{\sqrt{2\pi}\sqrt{\sigma_{L,y}^2 + \sigma_{e,y}^2}} \int\int\int \mathrm{d}x\mathrm{d}s\mathrm{d}ct \rho_{e,s}(s_1 - ct) \cdot$$
$$\frac{\exp[-\frac{(x\cos\theta - s\sin\theta)^2}{2\sigma_{e,x}^2}] \exp[-\frac{(x\cos\theta + s\sin\theta)^2}{2\sigma_{L,x}^2}] \exp[-\frac{(ct + s\cos\theta - x\sin\theta)^2}{2\sigma_{L,s}^2}]}{(2\pi)^{3/2}\sigma_{e,x}\sigma_{L,x}\sigma_{L,s}} \ . \tag{5.22}$$

Using:

$$s_1 - ct \rightarrow s' \ , \qquad s \rightarrow \frac{s' - x\sin\theta + ct}{\cos\theta}$$

and

$$\mathrm{d}x, \mathrm{d}s, \mathrm{d}ct \longrightarrow \mathrm{d}x, \mathrm{d}s', \mathrm{d}ct \qquad \text{(the variable change Jacobian is } 1/\cos\theta) \ ,$$

Eq. (5.22) can be rewritten as:

$$L = \frac{2N_e N_\gamma \cos\theta}{(2\pi)^2\sqrt{\sigma_{L,y}^2 + \sigma_{e,y}^2}\sigma_{e,x}\sigma_{L,x}\sigma_{L,s}} \int \mathrm{d}s' \rho_{e,s'}(s') \int\int \mathrm{d}x\mathrm{d}ct \exp[-\frac{(2ct - 2x\sin\theta + s')^2}{2\sigma_{L,s}^2}]$$
$$\exp[-\frac{(x\cos\theta - \tan\theta(ct - x\sin\theta + s'))^2}{2\sigma_{e,x}^2}] \exp[-\frac{(x\cos\theta + \tan\theta(ct - x\sin\theta + s'))^2}{2\sigma_{L,x}^2}] \ , \quad (5.23)$$

where the electron longitudinal distribution (that changes turn by turn) depends only on the variable s'. Eq. (5.23) can be integrated with respect to the other variables without knowing $\rho_{e,s'}$.

To symplify the previous expression, one can put:

$$ct - x\sin\theta + s' \longrightarrow z \ ,$$

and $\mathrm{d}x, \mathrm{d}ct \longrightarrow \mathrm{d}x, \mathrm{d}z$ (the variable change Jacobian is equal to 1).

Therefore:

$$L = \frac{2N_e N_\gamma \cos\theta}{(2\pi)^2\sigma_{L,s}\sigma_{L,x}\sigma_{e,x}\sqrt{\sigma_{L,y}^2 + \sigma_{e,y}^2}} \int \mathrm{d}s' \rho_{e,s'}(s') \int\int \mathrm{d}x\mathrm{d}z \exp[-\frac{(2z - s')^2}{2\sigma_{L,s}^2}]$$
$$\exp[-\frac{(x\cos\theta - z\tan\theta)^2}{2\sigma_{e,x}^2}] \exp[-\frac{(x\cos\theta + z\tan\theta)^2}{2\sigma_{L,x}^2}] \equiv \quad (5.24)$$
$$\equiv \int \mathrm{d}s' \rho_{e,s'}(s') L_b(s') \qquad .$$

In the program $L_b(s')$ is calculated turn by turn at each given s' value, using a double numerical integration.

For the $L_b(s')$ calculus, the integration borders have to be determined. The integration borders have been chosen using the property that the Gaussian function value is practically equal to zero for all the values that are distant more than 4 σ from its average value. In other words, the z value has been fixed in the range

$$-2\sigma_{L,s'} + \frac{s'}{2} < z < 2\sigma_{L,s'} + \frac{s'}{2} \ ,$$

and, at a given z, one integrates with respect to x. The integration borders for this latter integration have been chosen by studying the intersection between the two Gaussian functions that depend on x.

L is evaluated approximating Eq. (5.24) by a sum:

$$L = \int \rho_{e^-s'}(s')\mathrm{d}s' L_b(s') \simeq \sum_{s'_i} \rho_{e,s'}(s'_i) L_b(s'_i) \triangle s' \ . \tag{5.25}$$

To obtain the electron longitudinal density the macro-particle distribution has been divided in a number of bins. In such a way the bunch linear density at the center of the $i-th$ bin, $\rho_{e,s'}(s'_i)$, has been calculated as:

$$\rho_{e,s'}(s'_i) = \frac{N_m(s'_i)}{N_{macro} \triangle s'} \ , \tag{5.26}$$

where $N_m(s'_i)$ is the number of macro-particles in the i-th bin, N_{macro} is the total number of macro-particles in the bunch, and $\triangle s'$ is the bin length.

When L is known, according to Eq. (5.18), N_I can be obtained using the Compton scattering cross section (σ_C).The Compton scattering cross section has been calculated starting from the equations given in [30]:

$$\sigma_C[b] = \frac{0.031(m_e c^2)^2}{E_0^4 E_\gamma^3 \cos^2\theta}\{2E_0E_\gamma^2[(2E_0-\omega_M-\omega_m)(\omega_M-\omega_m)$$
$$+2E_0^2\log(\frac{E_0-\omega_m}{E_0-\omega_M})] + \frac{4E_0m_e^2c^4E_\gamma}{\cos^2\theta}[\omega_M-\omega_m+E_0\log(\frac{E_0-\omega_M}{E_0-\omega_m})]$$
$$+\frac{(m_ec^2)^4}{\cos^4\theta(E_0-\omega_m)(E_0-\omega_M)}[(\omega_M-\omega_m)(2E_0^2-E_0\omega_M-E_0\omega_m$$
$$+\omega_M\omega_m)+2E_0(E_0-\omega_M)(E_0-\omega_m)\log(\frac{E_0-\omega_M}{E_0-\omega_m})]\} \quad (5.27)$$

where E_γ is the photon initial energy and ω_m and ω_M are respectively the minimum and the maximum energy of the scattered photon [30]:

$$\omega_m = \frac{E_0^2E_\gamma}{m_e^2c^4}[1-\beta][1+\beta\cos(2\theta)] \quad (5.28)$$

$$\omega_M = \frac{E_0^2E_\gamma[1+\beta][1+\beta\cos(2\theta)]}{m_e^2c^4+2E_0E_\gamma[1+\beta\cos(2\theta)]} \quad (5.29)$$

where the relativistic β factor for the electrons has been used.

Using Eq. (5.26), Eq. (5.18) can be written as:

$$N_I = \sum_{s_i'}\frac{N_m(s_i')}{N_{macro}\triangle s'}L_b(s_i')\triangle s'\cdot\sigma_C \equiv \sum_{s_i'}N_{Ib}(s_i') \ . \quad (5.30)$$

$N_{Ib}(s_i')$ represents the number of interactions between the particles of the $i-th$ bin and the laser.

The scattered photon energy has been calculated applying the Von Newman's method to the distribution function that describes the final photon energy differential cross section [30]:

$$\frac{d\sigma}{dE_{\gamma'}}[\frac{b}{MeV}] = \frac{0.12475m_e^2c^4}{E_0^2E_\gamma\cos^2\beta}[1-\frac{E_{\gamma'}}{E_0}+\frac{E_0}{E_0-E_{\gamma'}}-$$
$$\frac{m_e^2c^4E_{\gamma'}}{E_0(E_0-E_{\gamma'})E_\gamma\cos^2\beta}(1-\frac{m_e^2c^4E_{\gamma'}}{4E_0^2(E_0-E_{\gamma'})E_\gamma\cos^2\beta})] \ , \quad (5.31)$$

where E_γ' is the scattered photon energy.

5.6.2 Laser effect on energy bunch distribution

The interaction between the electrons and the laser induces an energy spread in the bunch distribution.

The probability $P_e(s'_i)$ that an electron in the center of $i-th$ bin scatters off a laser photon is:

$$P_e(s'_i) = \frac{N_{Ib}(s'_i)}{N_e \rho_{e,s'}(s'_i) \triangle s'} \ , \tag{5.32}$$

where N_e is the number of electrons in the bunch, $N_{Ib}(s'_i)$ has been defined in Eq. (5.30), $\rho_{e,s'}(s'_i)$ and $\triangle s'$ have been defined in Eq. (5.26) (hence $N_e \rho_{e,s'}(s'_i) \triangle s'$ is approximatively the number of electrons in the $i-th$ bin). The interaction probability of an electron that is not in the center of the bin, is obtained by a linear interpolation on the $P_e(s'_i)$ of all the bins.

Taking into account the interaction probability, the P variable of each macro-particle changes according to:

$$P_{fin} = P_{in} + \frac{E_\gamma}{E_0} - \frac{E'_\gamma}{E_0} \ , \tag{5.33}$$

where E'_γ is the energy of the scattered photon, calculated as explained in the previous section.

5.7 Program tests

First, the reproduction by the program of the longitudinal beam dynamics without the interaction with the laser has been checked. In fact, in these conditions, the bunch longitudinal distributions have a Gaussian shape, whose standard deviations can be calculated theoretically [36]. It has been tested that the normalized particle distributions, with an initial rectangular profile, become Gaussian with respect to the variables P and Φ after three damping times.

The test of the program part simulating the interaction between beam and laser has been important because they have allowed to decide the macro-particle and bin number and to check the numerical integration used to cal-

culate $L_b(s')$. When also (in addition to the transverse electron distributions and to the transverse and longitudinal laser distributions) the longitudinal electron distribution is Gaussian (with standard deviation $\sigma_{e,s}$), the luminosity between the laser pulse and the electron bunch can be written as [30]:

$$L = \frac{N_e N_L}{2\pi\sqrt{\sigma_{e,y}^2 + \sigma_{L,y}^2}\sqrt{\cos^2(\theta)(\sigma_{e,x}^2 + \sigma_{L,x}^2) + \sin^2(\theta)(\sigma_{e,s}^2 + \sigma_{L,s}^2)}}\,, \quad (5.34)$$

where N_L is the amount of photons in one laser pulse and θ is half the crossing angle (between the laser pulse and the electron bunch). Therefore, when both the electron bunch and the laser pulse have Gaussian profiles it is possible to calculate N_I analytically, using Eqs. (5.18) and (5.34). The input parameters, used for the N_I calculus, are reported in Table 5.7.

N_e	10^{10}
N_L	10^{19}
E_γ(eV)	1.16
E_0(GeV)	1.3
$\sigma_{e,x}$(m)	25×10^{-6}
$\sigma_{e,y}$(m)	5×10^{-6}
$\sigma_{e,s}$(m)	1×10^{-3}
$\sigma_{L,x}$(m)	5×10^{-6}
$\sigma_{L,y}$(m)	5×10^{-6}
$\sigma_{L,s}$(m)	0.9×10^{-3}
θ	4°

Table 5.1: Input parameters used to test the program

With these input parameters the Compton cross section σ_C results to be 0.66 b and the analytical calculus gives $N_I = 1.54053 \times 10^9$.

As a check, this results was compared to the one given by the program in the same conditions.

The agreement between the analytical and numerical values improves by increasing the number of the macro-particles and of the bins. The error becomes negligible ($\sim 0.01\%$) for $N_{macro} = 10^5$ and a bin number equal to 100, that are still reasonable values in terms of computational time.

5.8 Simulation results

Initially, the program has been used to study longitudinal beam stability in the lattice with wigglers and with $E_0 = 1.3$ GeV (see C lattice configuration in Table 4.2).

To understand the main physical aspects of the single bunch dynamics in the Compton Ring, the simulations with the program have been made using only one laser cavity.

The bunch phase space has been studied, turning on the laser only for 100 or 200 turns: in the C configuration 200 turns correspond to a synchrotron period. The number of turns, in which the laser is turned on, has been related to the synchrotron period because the electron oscillations, around the synchronous one, can cause a misalignment between the bunch center and the laser pulse center. Therefore one expects that the number of interactions depends strongly on this misalignment [42].

Fig. 5.2 reports the bunch average value with respect to Φ ($\langle\Phi\rangle$) as a function of the number of turns (the laser is turned on for 200 turns).

The misalignment between the electron bunch and the laser pulse is also shown in Fig. 5.3 where one reports the $\langle\Phi\rangle$ and $\langle P\rangle$ (the bunch average value with respect to P) over 200 turns. In the figure, the dashed line indicates the laser pulse center. Because of the interaction with the laser, the bunch distributions are no longer Gaussian and the simulations foresee effects of bunch lengthening and bunch profile distortions. Fig. 5.4 reports the bunch

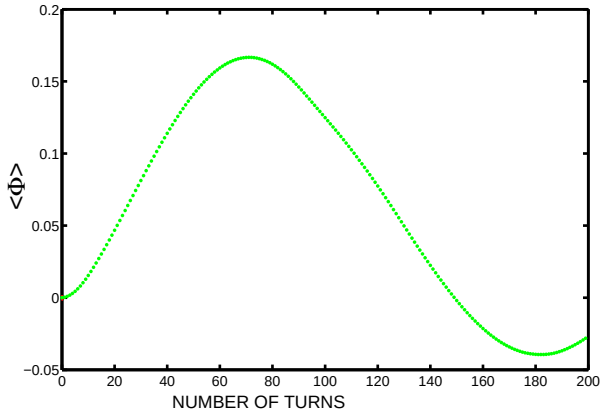

Figure 5.2: $\langle\Phi\rangle$ of the bunch as a function of the number of turns.

standard deviation with respect to Φ ($\Delta\Phi$), that is proportional to bunch length, as a function of the number of turns. The figure shows that the bunch lengthens because of the interaction with the laser.

Fig. 5.5 (on the left) shows the amount of photons, produced by the electron-laser interaction as a function of the turn number, in the case of the laser turned on for 200 turns. On the right of the same figure the photon number in the energy range 23-29 MeV are represented (23-29 MeV is the photon energy range proposed at Snowmass 2005 for the positron production in the target). There are two well defined peaks in the figure. The first peak corresponds to the beginning of synchrotron oscillation. The second peak corresponds to half synchrotron period. After the second peak a net decrease of the interaction number and the presence of a third peak by 200 turns were expected. However, as one can see in the figure, this is not the case. This can be explained taking into account the effects of the laser on the bunch distributions. In fact, the consecutive interactions with the laser cause a regime of instability characterized by the appearance of some spikes

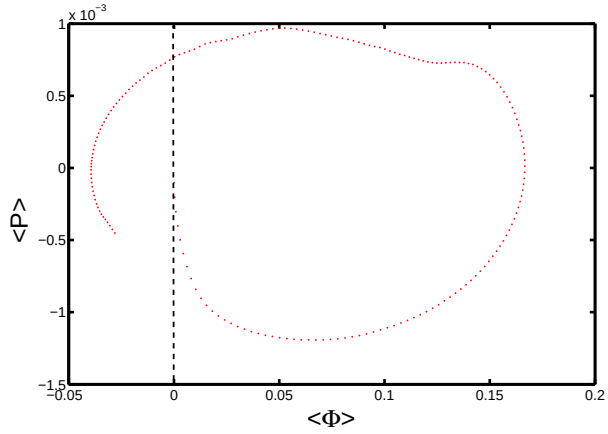

Figure 5.3: $\langle P \rangle$ and $\langle \Phi \rangle$ at different turns. The dashed line indicates the laser pulse center.

on the bunch distributions. These spikes increase progressively their height and change their position: this is the reason of the irregular behaviour of the number of interactions after about 120 turns, that therefore represents an instability threshold.

Fig. 5.6 shows the particle distribution with respect to Φ (on the left) and P (on the right) at different turns , with the laser turned on for 200 turns. The figure shows the distribution progressive distortion.

In order to study if the bunch distortions (induced by the laser) cause the bunch loss, after all the interactions with the laser, the bunch is allowed to continue turning in the ring (but with the laser turned off) for some damping times, so to verify if the bunch regained its equilibrium shape.

In Fig. 5.7 the longitudinal phase space is shown, at different turns, in the case, respectively, of the laser turned on for 100 and 200 turns.

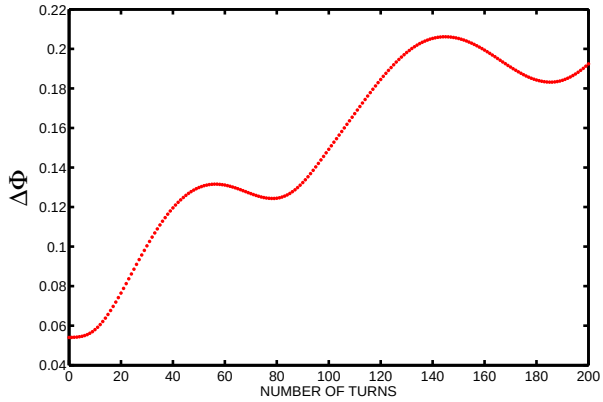

Figure 5.4: $\Delta\Phi$ as a function of the turn number.

Figs. 5.8 and 5.9 show the initial longitudinal phase space and after 4 damping times. The laser has been turned on for 100 and 200 turns respectively. It is interesting to note in Fig. 5.8 that, after 4 damping times, the bunch is totally regained. On the contrary, in Fig. 5.9, a part of the bunch is not able to return in the initial phase space with respect to the Φ coordinate. This is another evidence of the strong instability due to the laser in the case of 200 interactions.

Fig. 5.10 reports the energy distribution of the photons produced by Compton scattering at different turns. The plot shows that, for E_0 =1.3 GeV, the maximum energy of the scattered photons is $\sim$ 29 MeV; on the contrary, for $E_0 = 2$ GeV, the maximum energy is $\sim$ 45 MeV.

Other simulations have been done using the other CR lattices proposed in Chapters 3 and 4. All the lattices are characterized essentially by the same longitudinal beam dynamics. Anyway, some little quantitative differences can be put in evidence:

- the maximum energy of the scattered photons varies in the range 29-45 MeV;
- the synchrotron period varies in the range 150-200 turns;

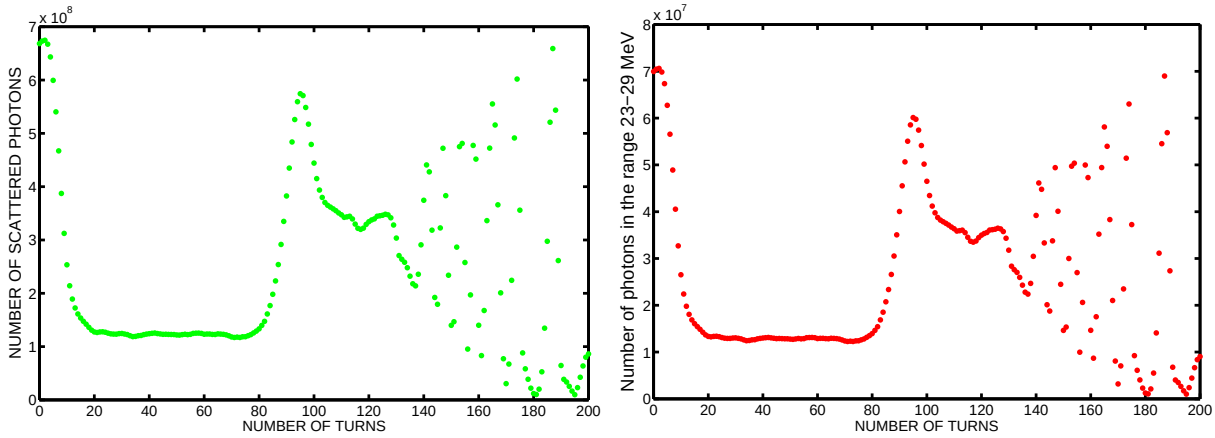

Figure 5.5: Total amount of photons (on the left) and number of photons in the energy range 23-29 MeV (on the right), produced by the electron-laser interaction as a function of the number of turns.

- the number of scattered photons varies by a factor of 1.05.

For example, it is interesting to compare Fig. 5.3 to Fig. 5.11 that shows the $\langle P \rangle$ and $\langle \Phi \rangle$ values at different turns with the laser turned on for 200 turns in the B' lattice of Table 4.3 (that has a synchrotron period of about 150 turns).

As a conclusion, the simulation results have shown that the lattices proposed in the previous chapters, allow to realize efficiently photo-production via Compton scattering. Furthermore choosing accurately the number of turns (depending on lattice features) over which the laser is turned on, it is possible to avoid that the instabilities induced by the electron-laser interaction cause the beam loss (thanks to the synchrotron radiation effects on bunch distribution when the laser is turned off). Using the lattice with the energy of 2 GeV (lattice B'), the maximum energy of the scattered photons is greater than that of the lattices with 1.3 GeV; anyway, also in this case, the results are encouraging because turning on the laser for ~ 60 turns (instead of ~ 100 turns as in the C lattice) it possible to avoid bunch loss.

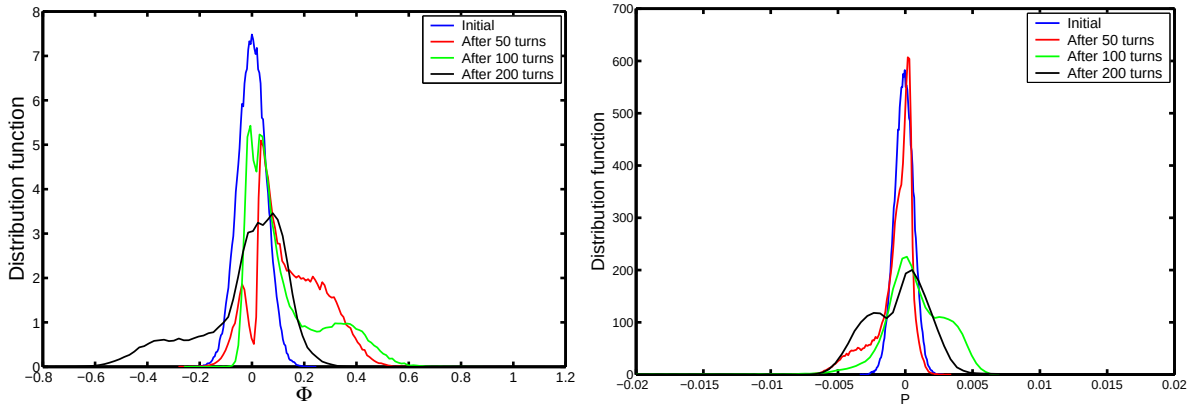

Figure 5.6: The particle distribution with respect to Φ (on the left) and P (on the right) at different turns, with the laser turned on for 200 turns.

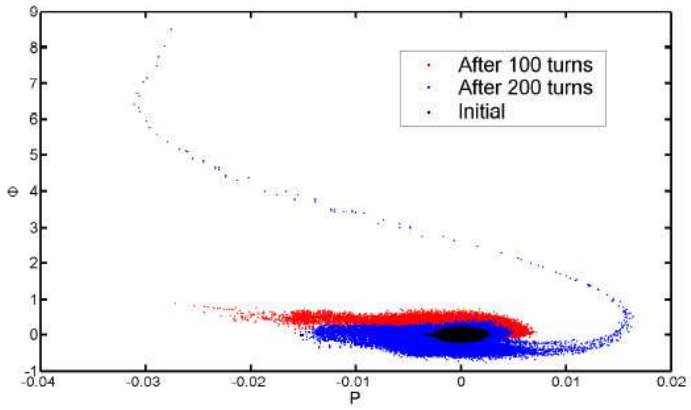

Figure 5.7: Initial longitudinal phase space and at different turns (with the laser turned on).

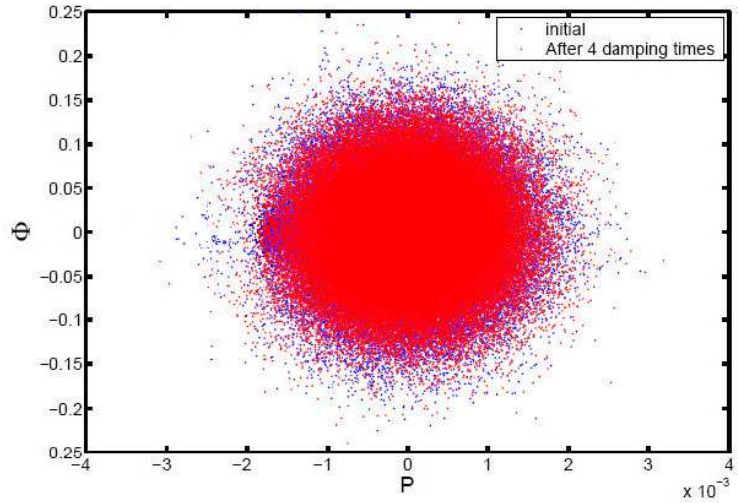

Figure 5.8: Initial longitudinal phase space and after 4 damping times, with the laser turned on for 100 turns.

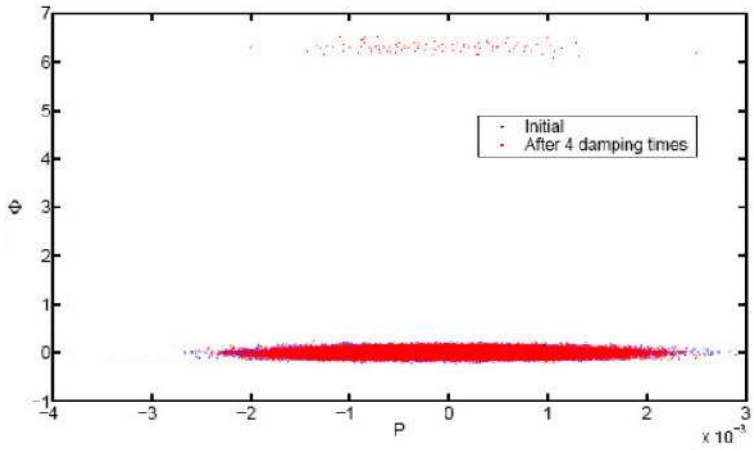

Figure 5.9: Initial longitudinal phase space and after 4 damping times, with the laser turned on for 200 turns.

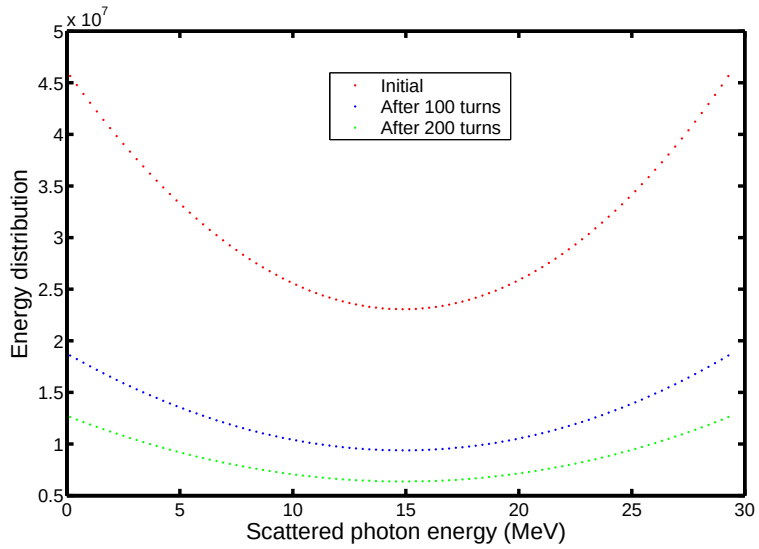

Figure 5.10: Energy distribution of the photons produced by Compton scattering at different turns.

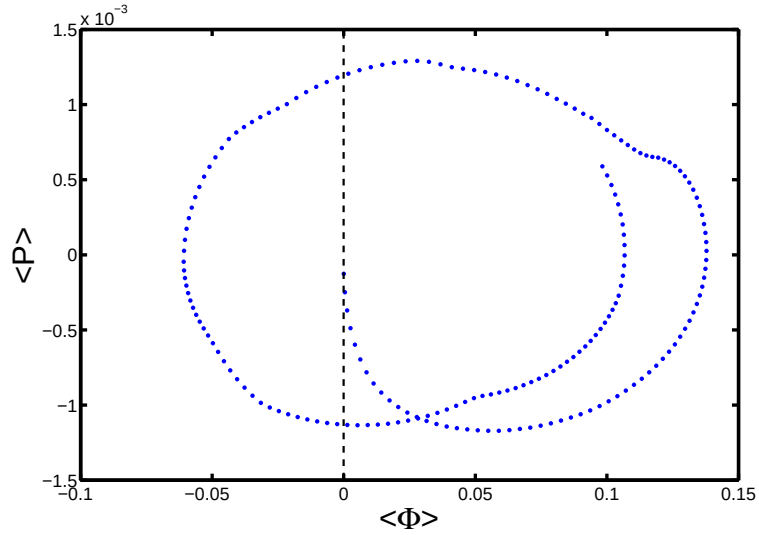

Figure 5.11: $\langle P \rangle$ and $\langle \Phi \rangle$ values with the laser turned on for 200 turns in the B' lattice configuration.

Chapter 6

Conclusions

In this thesis different models for the Compton Ring lattice have been presented. The lattice design studies have been done starting from the parameters (emittance, momentum compaction, bunch dimensions...) proposed at Snowmass 2005 Conference. The characteristics of the lattice have been modified with respect to Snowmass proposal to take into account different aspects of a realistic ring (circumference, beam life-time, dynamic aperture, cost...).

By mean of a simulation program this thesis shows the feasibility of the photo-production via the installation of laser cavities in the designed lattices. Anyway, the same simulation program has put in evidence the effects of the laser cavity on the longitudinal beam dynamics: bunch lengthening, misalignment between electron bunch and laser pulse, bunch distribution distortion, presence of spikes in the longitudinal distributions. These instabilities can be removed choosing accurately the amount of turns during which the laser is turned on. In fact, if this number is sufficiently short, the synchrotron radiation effects, when the laser is turned off, are able to restore the bunch natural Gaussian shape.

Therefore the results presented in this thesis are encouraging for a Compton source to polarize positrons at ILC. In fact, the studies of this thesis have shown the feasibility of a ring with the very low horizontal emittance ($\sim 10^{-10}$ m rad) and the low momentum compaction ($\sim 10^{-4}$) proposed at

Snowmass 2005 (see Table 2.1) and needed for the photo-production process via Compton scheme.

Anyway, several effects have to be still considered and a lot of upgrades can be done to improve the ring performances. One expects that the intrabeam scattering could be very strong and could cause emittance growth (in particular, in the low energy lattices [52]). Also collective effects [53] due either to the interaction with the vacuum chamber elements or to coherent synchrotron radiation (CSR) production [54] could cause beam instabilities or other effects leading to some changes in beam parameters (emittance growth, bunch lengthening,...). Recently it has been proposed [55] to apply the strong RF focusing principle [56] to the Compton Ring lattice. In a strong RF focusing regime, the bunch length is not constant along the ring: therefore it is possible to have a short bunch only in the machine regions where it is needed (in the Compton Ring a short bunch is needed only in the laser cavities). Having short bunches only in one machine region is particularly advantageous because the longitudinal collective instabilities, due to the CSR or the vacuum chamber, strongly depends on the bunch length average value along the ring [57]. The lattices presented in this thesis can be easily modified to realize an isochronous strong RF focusing regime taking to account the lattice studies presented in [58].

Appendix A

Touschek lifetime

A.1 Touschek scattering

Coulomb scattering between two particles of a bunch can cause the trasformation of their transverse momenta into longitudinal momenta. The particles are lost if this new momenta are outside the momentum acceptance. This effect is known as $Touschek\ effect$ because it was first studied by Bruno Touschek at the ADA storage ring of Frascati.

One can write the Coulomb differential cross section ($M\ddot{o}ller\ formula$) in the non-relativistic approximation for two particles with equal and opposite momenta:

$$\frac{d\sigma}{d\Omega} = \frac{4r_0^2}{(v/c)^2}[\frac{4}{sin^4\theta} - \frac{3}{sin^2\theta}] \ , \tag{A.1}$$

where r_0 is the classical electron radius, v is the relative velocity in the centre of mass system (CMS) and θ is the scattering angle.

The variable q can be introduced as:

$$q = \frac{p_x}{m_0 c} = \frac{1}{2}\frac{v}{c} \ , \tag{A.2}$$

which is a dimensionless momentum. In Eq. (A.2), p_x is the horizontal momentum of one particle. If one considers a flat beam the most important effect on the collision happens in the horizontal plane. After elastic collision between the two particles the momentum longitudinal components are

$q(m_0c)\cos\chi$ in the CMS (χ is the scattering angle with respect the nominal trajectory). Using Lorentz transformations in the hypotesis of non-relativistic motion in the CMS, the longitudinal momentum in the laboratory frame becomes:

$$p_s \simeq q(m_0c)\gamma\cos\chi \ . \tag{A.3}$$

The particle is lost if the longitudinal component is larger than the momentum acceptance Δp_{RF}. In other words it is needed that:

$$\mid \cos\chi \mid > \frac{\Delta p_{RF}}{\mid q \mid \gamma} \equiv \mu \tag{A.4}$$

The total cross section (in the CMS) can be written, using Eq. A.4, as:

$$\sigma = \frac{8\pi r_0^2}{(v/c)^4}[\frac{1}{\mu^2} - 1 + \log\mu] \tag{A.5}$$

A.2 Loss rate and lifetime

The differential loss rate of the particles is:

$$\mathrm{d}(\frac{\mathrm{d}N}{\mathrm{d}t}) = \sigma v \rho \mathrm{d}N \ . \tag{A.6}$$

where N is the number of particles in the bunch, σ is the cross section, v is the relative speed between the scattering particles and ρ is the particle density. Since incoming and scattered particles belong to the same ensemble, i.e. $\mathrm{d}N = \rho \mathrm{d}V$, one has:

$$\mathrm{d}(\frac{\mathrm{d}N}{\mathrm{d}t}) = \sigma v \rho^2 \mathrm{d}V \ . \tag{A.7}$$

The total loss rate is:

$$\frac{\mathrm{d}N}{\mathrm{d}t} = \bar{\sigma v} \int \rho^2 \mathrm{d}V \ , \tag{A.8}$$

where the approximation that σv does not depend on the particle coordinates has been done.

In the hypotesis of Gaussian distribution functions, in the transverse and longitudinal planes, the bunch volume is:

$$V_B = (4\pi)^{3/2}\sigma_x\sigma_y\sigma_s \tag{A.9}$$

The average $\sigma\bar{v}$ has to be done with regard to the change in a relative momentum which leads to particle loss:

$$\sigma\bar{v} = 2 \quad \int_{\frac{\Delta p_{RF}}{\gamma}}^{x} g(q)(\sigma_v)\mathrm{d}q \ , \tag{A.10}$$

where the factor two is due to the fact that the lost particles in each scattering process are two and

$$g(q) = \frac{1}{\sqrt{2\pi}\sigma_q}e^{-\frac{q^2}{2\sigma_q^2}}$$

with

$$\sigma_q = \frac{\gamma\sigma_x'}{\sqrt{2}} \ ,$$

where σ_x' is the beam angular divergence.

Using the quantities u and ϵ defined as:

$$u = (\frac{q}{\sigma_{px}})^2 \ , \qquad \epsilon = (\frac{\Delta p_{RF}}{\gamma\sigma_{px}})^2$$

(where σ_{px} is the horizontal momentum spread of electron beam in the unit of m_0c), the 'Touschek growth rate' $\frac{1}{\tau_T} = \frac{1}{N}\frac{dN}{dt}$ (τ_T is the Touschek lifetime) for a flat beam can be written as [51]:

$$\frac{1}{\tau_T} = \frac{\sqrt{\pi}r_0^2c}{\gamma^3}\cdot\frac{N}{V_B\sigma_x'}\cdot\frac{1}{(\frac{\Delta p_{RF}}{p_0})^2}$$
$$\{\epsilon\int_{\epsilon}^{\infty}\frac{1}{u^2}[(\frac{u}{\epsilon}) - \frac{1}{2}ln(\frac{u}{\epsilon}) - 1]e^{-u}du\} \ , \tag{A.11}$$

where the expression in the curly bracket is usually abbreviated by $C(\epsilon)$ and for $\epsilon < 1$ is approximated by:

$$C(\epsilon) = \log(\frac{1}{1.78\epsilon}) - 1.5 \ . \tag{A.12}$$

Appendix B

Particle motion in a circular accelerator

The trajectory equations (in linear approximation) in a circular accelerator with separated function magnets (the design orbit is assumed to be on the horizontal plane) are given by [40]:

$$\begin{aligned} x'' - (k - \tfrac{1}{\rho^2})x &= \tfrac{1}{\rho}\tfrac{\Delta p}{p_0} \\ z'' + kz &= 0 \end{aligned} \tag{B.1}$$

where x and z are the transverse coordinates (see Fig. B.1), ρ is the local radius of curvature (for a quadrupole $\rho = \infty$), g is the local field gradient (for a dipole $g = 0$), $p_0 = eB_0$ (B_0 represents the dipolar magnetic field), $k = \frac{eg}{p_0}$, $\Delta p = p - p_0$ (p is the particle momentum), the prime indicates the derivative with respect to the arc length s.

The term $\frac{1}{\rho^2}x$ describes the 'weak focusing' of a bending magnet, and k represents the 'strong focusing' given by the quadrupoles. In the very large high-energy accelerators $k >> \frac{1}{\rho^2}$. Eqs. (B.1) are known as *Hill equations*.

The equation for the horizontal motion can be written as:

$$x'' + K(s)x = \frac{1}{\rho} \cdot \frac{\Delta p}{p_0} \ , \tag{B.2}$$

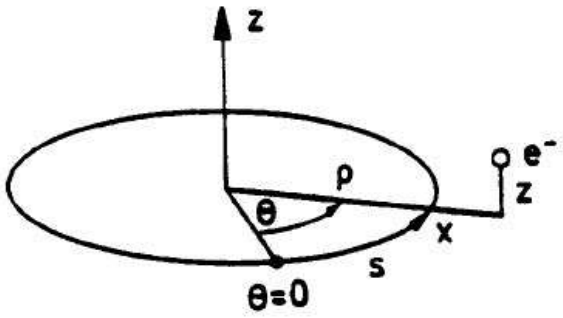

Figure B.1: Coordinats used to describe particle trajectories.

where

$$K(s) = -k(s) + \frac{1}{\rho^2(s)} \ .$$

The general solution for $x(s)$ is

$$x(s) = x_h(s) + x_i(s)$$

where x_h and x_i are respectively the homogeneous solution and the particular solution of the equation, i.e.

$$x_h'' + K(s)x_h = 0$$
$$x_i'' + K(s)x_i = \tfrac{1}{\rho}\tfrac{\Delta p}{p_0}$$

It is possible to introduce the function $D(s)$ to normalize x_i with respect to $\Delta p/p_0$:

$$D(s) = \frac{x_i}{\Delta p/p_0}$$

The general solution can be written as:

$$x(s) = C(s)x_0 + S(s)x_0' + D(s)\frac{\Delta p}{p_0} \tag{B.3}$$

with $x_0 = x_h(s_0)$ and $x_0' = x_h'(s_0)$. $C(s)$ and $S(s)$ are the so called Cosinelike and Sinelike solutions. These functions satisfy the equations:

$$C'' + K(s)C = 0 \ , \qquad S'' + K(s)S = 0$$

with

$$\begin{array}{ll} C_0 = 1 \ , & C_0' = 0 \\ S_0 = 0 \ , & S_0' = 0 \ . \end{array} \tag{B.4}$$

$D(s)$ is the dispersion function and it is defined as the solution of the equation:

$$D''(s) + K(s)D(s) = \frac{1}{\rho(s)} \tag{B.5}$$

with the initial conditions

$$D_0 = D_0' = 0 \ .$$

Hence one obtains the equation:

$$\begin{pmatrix} x \\ x' \end{pmatrix}_s = \begin{pmatrix} C & S \\ C' & S' \end{pmatrix} \begin{pmatrix} x \\ x' \end{pmatrix}_{s_0} + \frac{\Delta p}{p_0} \begin{pmatrix} D \\ D' \end{pmatrix} \tag{B.6}$$

that one can write as:

$$\begin{pmatrix} x \\ x' \\ \frac{\Delta p}{p_0} \end{pmatrix}_s = \begin{pmatrix} C & S & D \\ C' & S' & D' \\ 0 & 0 & 1 \end{pmatrix} \begin{pmatrix} x \\ x' \\ \frac{\Delta p}{p_0} \end{pmatrix}_{s_0} \tag{B.7}$$

The vertical motion is described by an equation as Eq. (B.6), but without the last term.

The dispersion trajectory expression, in terms of $C(s)$ and $S(s)$, is:

$$D(s) = S(s) \int_{s_0}^{s} \frac{1}{\rho(t)} C(t)dt - C(s) \int_{s_0}^{s} \frac{1}{\rho(t)} S(t)dt \ . \tag{B.8}$$

The matrix

$$M(s) = \begin{pmatrix} C & S \\ C' & S' \end{pmatrix} \tag{B.9}$$

is called $transfer\ matrix$.

It can be shown that, to have a stable trajectory, $M(s)$ can be written in the Twiss form:

$$M(s) = \begin{pmatrix} 1 & 0 \\ 0 & 1 \end{pmatrix} \cos\mu + \begin{pmatrix} \alpha(s) & \beta(s) \\ -\gamma(s) & -\alpha(s) \end{pmatrix} \sin\mu \tag{B.10}$$

where α, β, γ and μ are the Twiss parameters with

$$\alpha(s+L) = \alpha(s)\ , \qquad \beta(s+L) = \beta(s)\ , \qquad \gamma(s+L) = \gamma(s) \tag{B.11}$$

and μ indipendent on s. α, γ and μ can be written in terms of the betatron function β using the following relationships:

$$\beta\gamma - \alpha^2 = 1\ , \qquad \alpha(s) = -\frac{1}{2}\beta'(s)\ , \qquad \mu = \int_s^{s+L} \frac{dt}{\beta(t)}\ . \tag{B.12}$$

μ is known as the phase advance per period of length L.

The Floquet theorem [40] shows that the most general solution of the Hill equation is a pseudo harmonic oscillation of the form:

$$y_{1,2}(s) = a\sqrt{\beta(s)}e^{\pm i\phi(s)}\ , \tag{B.13}$$

where $y = x, z$, $\phi'(s) = 1/\beta(s)$ and a is a constant.

The oscillation amplitude and wavelength depend on the coordinate s and are both given in terms of the betatron function:

$$\text{amplitude} \propto \sqrt{\beta(s)}\ , \qquad \lambda(s) = 2\pi\beta(s)\ . \tag{B.14}$$

The Q (tune) value is defined as the number of the betatron oscillations per revolution. If the accelerator has N periods, Q is given by:

$$Q = \frac{N\mu}{2\pi}\ . \tag{B.15}$$

The area of the phase space ellipse is an important quantity. In fact this area remains invariant when one transforms the particle trajectories

through the accelerator. In the cartesian coordinate representation the ellipse equation is:

$$\gamma y^2 + 2\alpha y y' + \beta y'^2 = const. \tag{B.16}$$

also called 'Courant-Snyder' invariant. Hence the area of the ellipse enclosing the beam in phase space is also an invariant and it is the so called emittance ϵ. As it has been explained in Chapter 3, the horizontal and vertical emittances depend on the lattice style.

Appendix C

Beam properties due to wigglers

Wiggler position determines the growth or the fall of beam emittance. In particular, if wiggler is in a region with the dispersion function $D \neq 0$ beam emittance will increase; on the contrary, if wiggler is in a region with $D = 0$, beam emittance will decrease. To understand this effect one has to deal with damping wigglers, which in general contribute to all the synchrotron radiation integrals (as shown in [41], all the quantities related to synchrotron radiation, like the energy radiated or bunch dimensions, can be expressed using these integrals):

$$\begin{aligned} I_2 &= \int \frac{1}{\rho^2} ds \\ I_3 &= \int \frac{1}{|\rho|^3} \\ I_4 &= \int \frac{(1-2n)D(s)}{\rho^3} ds \\ I_5 &= \int \frac{H}{|\rho|^3} \end{aligned} \tag{C.1}$$

where $n = \frac{dB}{dx}\frac{\rho}{B_0}$, $H = \frac{1}{\beta(s)}[D(s)^2 + (\beta(s)D'(s) - \frac{1}{2}\beta'(s)D(s))^2]$ and the integrals have to be done along the machine.

It is possible to put in evidence the wiggler effect on the equilibrium energy spread (σ_ϵ) by the ratio [38]:

$$\frac{\sigma'_\epsilon}{\sigma_\epsilon} = [\frac{1 + I_3^{ID}/I_3}{1 + (2I_2^{ID} + I_4^{ID})}/(2I_2 + I_4)]^{1/2} \ , \tag{C.2}$$

where the wiggler (Insertion Device) contributions to the integrals are labelled as ID and σ'_ϵ is the energy spread taking into account wiggler contribution. For a sinusoidal field variation these contributions can be written as:

$$I_2^{ID} = \frac{L}{2\rho_{ID}^2} \qquad I_3^{ID} = \frac{4}{3\pi}\frac{L}{\rho_{ID}^3} \qquad I_4^{ID} = -\frac{1}{32\pi^2}\frac{\lambda_0^2}{\rho_{ID}^4}L \ , \tag{C.3}$$

where L is the length of the ID, λ_0 the period length and ρ_{ID} is the bending radius corresponding to the peak field of the ID. The I_4^{ID} term is the so called self-dispersion. In most cases this term is negligible compared to the larger I_2^{ID} term (and I_4 is negligible with respect to I_2). If one considers the isomagnetic lattice case, Eq. (C.2) can be symplified :

$$\frac{\sigma'_\epsilon}{\sigma_\epsilon} = [\frac{1 + \frac{4}{3\pi}\frac{L}{2\pi\rho}(\frac{\rho}{\rho_{ID}})^3}{1 + \frac{1}{2}\frac{L}{2\pi\rho}(\frac{\rho}{\rho_{ID}})^{1/2}}]^{1/2} \tag{C.4}$$

From the previous equation one can note that if the peak field in the ID is less than that of the bending magnets ($\rho_{ID} < \rho$), there is a reduction of energy spread. On the contrary, if the peak ID field exceeds the bending magnet field ($\rho_{ID} > \rho$), the energy spread increases.

In the case of the emittance there is a complication: in fact the ID self-dispersion must be added to the dispersion that is present in the straight section without the ID:

$$D(s) = (\frac{\lambda_0}{2\pi})^2\frac{1}{\rho_{ID}}cos(\frac{2\pi s}{\lambda_0}) \qquad D'(s) = (\frac{\lambda_0}{2\pi})\frac{1}{\rho_{ID}}sin(\frac{2\pi s}{\lambda_0}) \tag{C.5}$$

If the dispersion in the straight section is large one can write, for the isomagnetic case:

$$\frac{\epsilon'_{x_0}}{\epsilon_{x_0}} = \frac{1 + \frac{4}{3\pi}\frac{L}{2\pi\rho}(\frac{H_{ID}}{H})(\frac{\rho}{\rho_{ID}})^3}{1 + \frac{1}{2}\frac{L}{2\pi\rho}(\frac{\rho}{\rho_{ID}})^2} \tag{C.6}$$

From the previous equation one can note that the emittance can be increased or decreased depending on the relative value of H and ρ in the insertion device and in the bending magnets. In particular, if H/ρ in the ID exceeds H/ρ in the bending magnets then the emittance will be increased. To have a low emittance, the insertion devices are placed in straight sections with zero dispersion. In this last case the self-generated dispersion in the ID dominates. The largest involved term is:

$$I_5^{ID} = \frac{\lambda_0^2}{15\pi^3\rho_{ID}^5}\langle\beta_x\rangle L \tag{C.7}$$

Except for very high field devices in low emittance and low energy rings the emittance is reduced by the ID. In fact, a condition to not increase the emittance is:

$$\lambda_0^2 B^3 \leq 5.87 \times 10^9 \frac{E[GeV]\epsilon_{x_0}}{\langle\beta_x\rangle} \ , \tag{C.8}$$

where E is the particle energy.

Increasing $\int B^2 ds$ in the wigglers, it is possible to achieve in the same time a short damping time and a low beam emittance. In fact:

$$\tau \propto \frac{T_0}{E\int B^2 ds} \qquad \epsilon \propto \frac{E}{\int B^2 ds} \tag{C.9}$$

where T_0 is the revolution period and B represents the magnetic field. To reduce the wiggler emittance three methods can be utilized:

- Long wiggler with low field;
- Short period;
- Small average beta.

The first method implies a smaller rms relative energy spread σ_ϵ. An other implication is the reduction of the synchrotron radiation power emitted per unit length. To reduce the average beta $\langle\beta\rangle$ one can:

- increase the strength of the quadrupoles (increasing chromaticity);
- reduce the wiggler length (increasing cost).

Acknowledgements

My work is finished... fortunately and unfortunately! This year has been very hard and difficult but I have learnt many things; not only about accelerator physics. I am happy because a new period of my life will begin but I am closing an important period of my youth.

I came in Pisa five years ago and I will remember every moment for ever. I want to thank my family: my dad Tonino, my mom Teresa, my sisters Daniela, MariaTeresa and Martina, and my brother Alfredino. They have put faith in me and I have ever thought about them in all the difficult moments.

I want to thank my uncles, my cousins and my grandparents, because every time I come back in Calabria it seems like I have never gone away.

I want to thank very special people... Enza, Cecilia, Andrea, Edoardo, Sophia, Elisa, Lara. I will carry them in my hearth for all my life.

I want to thank my supervising professor, Prof. Franco Cervelli, for his patience and availability, and Dr. Susanna Guiducci, because she has had confidence in me and she has taught me many things. I want to acknowledge Dr. Caterina Biscari and Dr. Andra Ghigo for their help and their interest with respect to my studies and my future. A particular acknowledgement to Dr. David Alesini for his friendship and to Dr. Manuela Boscolo, for her hospitality and for her precious advices.

Finally I want to speak about my future, that is Luciano. I have not words to thank him for his help and his support. I can only say that I love him and I can not think about my days without him.

Bibliography

[1] J. A. Aguilar-Saavedra et al. [ECFA/DESY LC Physics Working Group], eds. R.- D. Heuer, D. Miller, F. Richard and P. Zerwas, arXiv:hep-ph/0106315; F. Richard, J. R. Schneider, D. Trines and A. Wagner, arXiv:hep-ph/0106314

[2] T. Abe et al. [American Linear Collider Working Group Collaboration], in Proc. of the APS/DPF/DPB Summer Study on the Future of Particle Physics (Snowmass 2001) ed. N. Graf, SLAC-R-570 Resource book for Snowmass 2001, 30 Jun - 21 Jul 2001, Snow- mass, Colorado; hep-ex/0106055, hep-ex/0106056, hep-ex/0106057, hep-ex/0106058; K. Abe et al. [ACFA Linear Collider Working Group Collaboration], arXiv:hepph/ 0109166; K. Abe et al., KEK-REPORT-2003-7

[3] F. Zimmermann, CLIC scheme of polarized positron source based on laser Compton scattering, Abstracts of POSIPOL 2006, CERN, Switzerland

[4] ICFA, Parameters for the Linear Collider, see webpage: www.interactions.org/linearcollider/documents/index.htm

[5] G. Moortgat-Pick et al., The role of polarized positrons and electrons in revealing fundamental interactions at the Linear Collider, arXiv:hep-ph/0507011 v1 1 Jul 2005

[6] S.Heinemeyer, S. Kraml,W. Porod and G.Weiglein, JHEP 0309 (2003) 075 [arXiv:hepph/ 0306181]; G.Weiglein, Nature 429 (2004) 613

[7] J. H. Kuhn, LC-TH-2001-004; M. Jezabek, Nucl. Phys. Proc. Suppl. 51C (1996) 60; R. Harlander, M. Jezabek, J. H. Kuhn and M. Peter, Z. Phys. C 73 (1997) 477 [arXiv:hep-ph/9604328]

[8] B. Grzadkowski and Z. Hioki, Nucl. Phys. B 585 (2000) 3 [arXiv:hep-ph/0004223]

[9] J. A. Aguilar-Saavedra and T. Riemann, arXiv:hep-ph/0102197

[10] E. W. N. Glover et al., Acta Phys. Polon. B 35 (2004) 2671 [arXiv:hep-ph/0410110]; J. A. Aguilar-Saavedra, Acta Phys. Polon. B 35 (2004) 2695 [arXiv:hep-ph/0409342]

[11] M. Diehl, O. Nachtmann and F. Nagel, Eur. Phys. J. C 27 (2003) 375 [arXiv:hepph/ 0209229]

[12] J. Fleischer, K. Kolodziej and F. Jegerlehner, Phys. Rev. D 49, 2174 (1994)

[13] R. Hawkings and K. Monig, Eur. Phys. J. directC 1 (1999) 8 [arXiv:hep-ex/9910022]; K. Monig, LC-PHSM-1999-2-TESLA

[14] E. Boos, H. U. Martyn, G. Moortgat-Pick, M. Sachwitz, A. Sherstnev and P. M. Zerwas, Eur. Phys. J. C 30 (2003) 395 [arXiv:hep-ph/0303110

[15] H. E.Haber and G. L. Kane, Phys. Rept. 117 (1985) 75; J. Gunion, H. E.Haber, G. Kane and S. Dawson, The Higgs Hunters Guide, Addison-Wesley 1990

[16] U. Ellwanger, J.-F. Gunion and C. Hugonie, arXiv:hep-ph/0503203

[17] G. F. Giudice, R. Rattazzi and J. D. Wells, Nucl. Phys. B 544 (1999) 3 [arXiv:hepph/ 9811291]

[18] T. Han, J. D. Lykken and R. J. Zhang, Phys. Rev. D 59 (1999) 105006 [arXiv:hepph/ 9811350]

[19] G. W. Wilson, Study of the sensitivity to extra dimensions in the photon graviton channel with polarised beams, LC-PHSM-2001-010

[20] L. Vacavant and I. Hinchliffe, arXiv:hep-ex/0005033

[21] S. Cullen,M. Perelstein and M. E. Peskin, Phys. Rev. D 62 (2000) 055012 [arXiv:hepph/ 0001166]

[22] H. Grote, F. C. Iselin, The MAD program, user's reference manual, CERN/SL/90-13 (AP)

[23] R. Alley et al., The Standford Linear Accelerator Polarized Electron Source, Nucl.Inst. and Meth. A365, (1995)

[24] A.A. Mikhailichenko and V.E. Balakin, Conversion sistem for obtaining polarized electrons and positrons at high energy, CBN 02/13 (1979)

[25] K. P. Schuler, Polarimetry of polarized positrons, Posipol06 Workshop CERN, 26-28 April 2006

[26] V.N. Bayer, V.N.Katkov, V.S. Fadin, Radiation of Relativistic Electrons, AtomIzdat, M., 1973

[27] D. Perkins, Introduction into High Energy Physics, ed. by Yu.A. Budanov, Mir, Moscow, 1975

[28] A.D. Bukin, A.A. Mikhailichenko, Optimized Target Strategy for Polarized Electrons/Positrons production for Linear Collider, Budker INP 92-76, Novosibirsk, 1992

[29] A. Mikhailichenko, Liquid metal target for ILC, Proceedings of EPAC'06

[30] J. Yang, M. Washio, A. Endo, T. Hori, Nucl. Instr. and Meth. in Phys. Res. A 428, 556-569 (1999)

[31] E. Esarey, S.K. Ride, P. Sprangle, Phys. Rev. E 48 (1993) 3003

[32] G. Alexander et al., E-166 collaboration, SLAC-TN-04-018, LC-DET-2003-044

[33] A. Kh. Khokonov and M. Kh. Khokonov, Classification of the interactions of relativistic electrons with laser radiation., Technical Physics Letters, 31(2):154156, 2005

[34] I. Sakai et al., Phys. Rev. ST Accel. Beams 6 (2003) 091001

[35] T. Omori et al., PRL 96 (2006) 114801

[36] M. Sands, The physics of electron storage rings: an introduction, SLAC-121 UC-28

[37] R.P. Walker, Radiation damping, Proceedings of the fifth general Accelerator Physics course, CERN (1992)

[38] R.P. Walker, Quantum excitation and equilibrium beam properties, Proceedings of the fifth general Accelerator Physics course, CERN (1992)

[39] E. Bulyak, P. Gladkikh, V. Skomorokhov, Synchrotron dynamics in Compton x-ring with nonlinear momentum compaction, http://arXiv:physics/0505204 v1 (2005)

[40] J. Rossbach, P.Schmüser, Basic course on accelerator optics, Proceedings of the fifth general Accelerator Physics course, CERN (1992)

[41] R. H. Helm, M. J. Lee, P. L. Morton, Evaluation of synchrotron radiation integrals, SLAC-PUB-1193 (1973)

[42] S. Araki et al., Conceptual design of a polarized positron source based on laser Compton scattering, http://arXiv:physics/0509016 v1 (2005)

[43] A. Ropert, Lattice and Emittance, ESRF, Grenoble, France

[44] W. Decking, Optical layout of the TESLA 5 GeV Damping Ring, DESY, Hamburg, Germany

[45] R.P. Walker, Wigglers, CAS, CERN

[46] A. Wolsky, Damping ring design, Lecture at the ILC school, 19-27 May 2006, Japan

[47] A. Wolsky, J. Gao, S. Guiducci, Configuration studies and recommendations for the ILC Damping Rings, LBNL59449

[48] S. Guiducci, Chromaticity, Proceedings of the fifth general Accelerator Physics course, CERN (1992)

[49] E. Wilson, Transverse beam dynamics, Proceedings of the fifth general Accelerator Physics course, CERN (1992)

[50] D. Alesini, M. E. Biagini, A. Gallo, P. Raimondi, M. Zobov, Estimate of hourglass effect in Dafne, LNF-TECH. NOTE: G-62 (2004)

[51] A. Wrulich, Single beam life-time, CERN 94-01 (1994)

[52] S. Guiducci, E. Bressi , Lattice design for Compton ring, Abstracts of POSIPOL 2006, CERN, Switzerland

[53] A. Chao , Coherent instabilities on a relativistic bunched beam, SLAC-PUB-2946, 1982

[54] M. Borland,Phys.Rev.ST Accel.Beams 4, 070701(2001)

[55] E. Bulyak, P. Gladkikh, Longitudinal Low-Beta Insertion for the Compton Rings, May 2006

[56] A. Gallo, P.Raimondi, M. Zobov e-Print Archive: physics/0404020

[57] L. Falbo, D. Alesini, M. Migliorati, Longitudinal beam dynamics in electron rings in SRFF regime, Proceedings of EPAC06, Edimburgh

[58] C. Biscari, Bunch length modulation in highly dispersive storage rings, Physical Review ST-AB, 8, 091001 (2005)

[59] J. Urakawa, The ILC Compton scheme, Abstracts of POSIPOL 2006, CERN, Switzerland